Parker Solar Probe FIELDS instrument charging in the near Sun environment: Part I – Computational Model

M.F. Diaz-Aguado[1], J.W. Bonnell[2], S. D. Bale[3] , J. Wang[4] and M. Gruntman[4]

[1]Millenium Engineering and Integration, NASA Ames Research Center, Moffett Field, California, USA

[2]Space Sciences Lab, University of California Berkeley, Berkeley, California, USA

[3]Department of Physics, University of California Berkeley, Berkeley, California, USA

[4] Astronautical Engineering Department, University of Southern California, Los Angeles, California, USA

Corresponding author: Millan Fernando Diaz-Aguado (millan.f.diaz-aguado@nasa.gov)

Key Points:

- We predict the floating potentials of the Parker Solar Probe spacecraft and FIELDS antennas using the SPIS particle-in-cell model
- We used laboratory evaluation of photoelectron and secondary electron properties of exposed surfaces
- We predict electrostatic barriers forming near the illuminated surfaces of the FIELDS antennas and shields.

Abstract

The Spacecraft Interaction Plasma Software package (SPIS), a three-dimension particle in cell (PIC) code, was used to model the Parker Solar Probe (PSP) spacecraft and FIELDS instrument and their interactions with the Solar wind. Our SPIS modeling relied on material properties of new spacecraft materials that we had obtained in previous work. The model was used to find the floating potentials of the spacecraft and FIELDS antennas at different distances from the Sun (from 1AU to 0.046AU). We find the following results: At greater distances from the Sun, the shadowed spacecraft charges negatively while the illuminated Thermal Protection System (TPS) charges positive due to the high resistance of the TPS Alumina shield at low temperatures. As the spacecraft approaches the Sun, the temperature of the TPS increases, the resistance between it and the spacecraft drops, and its photoemission increases, driving the spacecraft more positive. At the same time, an electrostatic barrier forms near the illuminated surface of the TPS and reflects the photoelectrons back leading to negative charging of some surfaces. The FIELDS antennas and shield also see this barrier forming but on a smaller scale. The FIELDS antennas charge positively at all distances modeled when no current bias is applied. Current biasing of the antennas affects their floating potential.

Plain Language Summary

Measuring the electric field in a space plasma is important for understanding how plasma flows are driven, charge particles are accelerated and heated, and electromagnetic waves propagate. Measuring the voltage difference between two spatially separated electrodes immersed in a space plasma is one way to estimate the electric field that is present in the plasma. Interpretation of these voltage differences is complicated by the fact that the electrodes often float at a significant voltage relative to the nearby plasma so as to achieve current balance between the electrode and the charged particle environment around it. Different surfaces will float to different potentials depending upon their surface materials, their location relative to other surfaces, their orientation with respect to the incident Sun's light and solar wind flows, and numerical modeling is required to predict how all these factors influence what is observed.

1 Introduction

Langmuir Probes have been used extensively in space missions to measure the density and plasma potential variations of the environment with respect to the probes [*Mott-Smith et al. '26, Garrett '81, Whipple '81, Gurnett et al. '95, Gustafsson et al. '97, Gurnett et al. '04, Vaivads et al. '07, Bonnell et al. '08, Wygant et al. '13, Andersson et al. '15, Bale et al. '16, Torbert et al. '16*]. To interpret Langmuir prove measurements, it is important to be able to measure and predict the plasma effects on the instrument and spacecraft charging environment [*Feuerbacher et al. '72, Grard '73, Whipple '81, Mullen et al. '86*]. Knowledge of the photoemission (photon induced electron emission from a surface), secondary electron emission (electron or ion induced electron emission from surface), backscattered electrons, and thermionic emission (electrons leaving the surface due to high surface temperatures) are crucial to understand the charging behavior of the probes.

The NASA Parker Solar Probe (PSP) is a mission to study the Sun. The instruments onboard PSP include the FIELDS instrument which measures the magnetic fluctuations and electric fields, plasma wave spectra and polarization properties, the spacecraft floating potential and solar radio emissions[*Bale et al. '16*]. PSP is currently operating at distances between 1AU and 0.16 AU away from the Sun, but its closest approach will be 0.046 AU. Due to this large range of heliocentric distances experienced by PSP, the environments and surface charging physics interactions also vary greatly. At the closest approach to the Sun, the FIELDS antennas are exposed to over 500 times the radiant photon flux present at 1 AU, driving proportionally greater magnitudes of photoelectron emission. These high fluxes drive the temperatures of illuminated surfaces to new extremes as well. For example, at closes approach, the FIELDS electric antenna system is required to operate at temperatures above 1570 K (4 times greater than that at 1AU). The FIELDS instrument alos must operated over a wider range of ambient plasma conditions, covering solar wind (SW) plasma densities ranging from 7 cm^{-3} to 4000 cm^{-3}, and electron and ion temperatures stretching from 8eV to 90 eV. At the closest approach, the SW density is about 580 times greater than that at 1AU (60 times greater than ever encountered by a spacecraft in the SW). This is a new operating (and survival) regime for this sort of instrument and presents several design and operational challenges. This paper studies the FIELDS antennas, the PSP thermal shields, and their interaction with each other and the environment. It also looks at a closer distance to the Sun of 9.5Rs, but the current mission's closest approach will be at 9.8Rs.

Figure 1 shows a rendering of the PSP spacecraft and elements of the FIELDS instrument. Previous PSP spacecraft surface charging models involved the PSP spacecraft, including the Thermal Protection System (TPS), the spacecraft radiators, and the bus. However, they did not include the FIELDS antennas [*Donegan et al. '10*, *Ergun et al. '10*, *Guillemant et al. '12, Donegan et al. '14*] because the necessary information to model the antennas, such as probe surface properties were not available, and the final geometry of these thin (0.0031m diameter) 2m long probes were unknown at the time of their publishing.

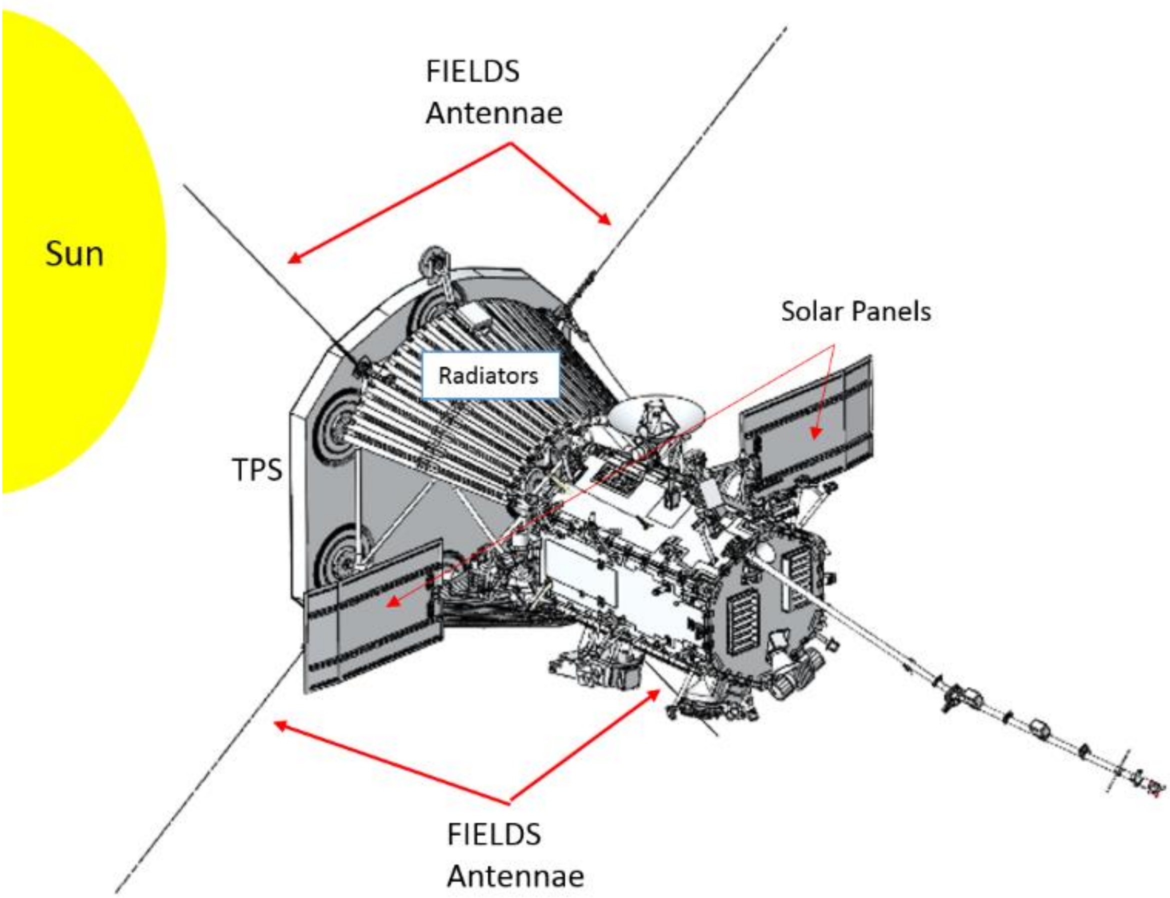

Figure 1 – CAD rendering of PSP with FIELDS Antennae deployed.

Throughout the entire mission, PSP slowly decreases its perihelion, getting closer to the Sun with each Venus encounter [*Fox et al. '16*]. The maximum illuminated surface temperatures rise with each pass, annealing and "baking out" those surfaces, leading to subtle changes in the spacecraft and antenna charging behavior. In addition, the solar photon flux changes as ~$1/R^2$ over each orbit, where R is the distance from the Sun [*Ergun et al. '10*], leading to significant changes in photoemission between aphelion and perihelion, and over the course of the mission.

In order to survive and operate at the high temperatures expected at perihelion, the PSP FIELDS antennas utilize for the first time a refractory Niobium alloy, Nb-C103. A testing campaign [*Diaz-Aguado et al. '19*, *Diaz-Aguado et al. '20*] quantitatively characterized the physical process involved and determined the charging properties of this new material, along with other refractory materials that were used on other parts of the FIELDS antennas. This test campaign obtained the material properties for photoemission, secondary electron (SE) emission and backscattered SE emission, properties needed to correctly model spacecraft and antenna charging.

A self-consistent modeling of plasma interactions with the spacecraft, taking into consideration the actual spacecraft configuration, is needed in order to predict the FIELDS antenna charging correctly. Many spacecraft-plasma interaction software models exist, including: EMSES, iPic3D, LASP, PTetra, Multiutility Spacecraft Charging Analysis Tool (MUSCAT), NASA Charging Analyzer Program (NASCAP)[*Mandell et al. '05*] and Spacecraft Plasma Interaction Software package SPIS [*Roussel et al. '08*, *Marchand et al. '14*]. This study utilized SPIS because it’s an open source design allows for ready inclusion of the novel material properties and surface geometries of the PSP FIELDS antennas and spacecraft.

The main purpose of this paper is to evaluate the charging environment of the PSP FIELDS antennas and quantify its effect on measurements of the SW plasma structure and dynamics by presenting the results of the SPIS model at close encounters and by comparing the model results with 1AU. First the spacecraft charging theory is described, including photoemission, SE emission, BSE emission, and thermionic emission. Electron and ion current theories are also included. Second, an overview of SPIS is provided, followed by environments explored and materials used specific to FIELDS and PSP. Finally, the model results are discussed.

2 Spacecraft Charging Overview

In steady state the spacecraft’s antenna floating potential is determined by the balance of various charging currents to and from the spacecraft or probe. The floating potential of a spacecraft or probe relative to the ambient plasma is determined by the current balance condition, that is the net current to any exposed surface must sum to zero. [*Whipple '65, Grard '73, Garrett '81, Whipple '81, Mullen et al. '86, Hastings et al. '96*]. For PSP these currents are determined by the SW plasma environment, solar photon flux, spacecraft orientation and material properties, which depend on the floating potential. PSP is designed to be electrically conductive between all surfaces during perihelia to obtain similar potentials throughout the spacecraft, except for specific instrumentation, including the FIELDS antennas and shields that remain isolated to make electric field measurements possible.

The current balance condition for PSP and FIELDS is

$$I(\Phi) = I_{ph}(\Phi) + I_I(\Phi) + I_{se}(\Phi) + I_{bse}(\Phi) + I_e(\Phi) + I_{therm}(\Phi) + I_{other} = 0 \quad (1)$$

where I_{ph} is the photoelectron current from photoelectron emission, I_I and I_e are the ion current and electron current from the plasma environment, respectively, I_{se} secondary electron current, and I_{bse} backscattered secondary electron current resulting from the electrons leaving a surface due to the plasma interaction with surfaces, I_{therrm} thermionic electron current from electrons emitted from a hot body, and I_{other} could be other currents such as sensor bias currents. Each of the currents varies with the spacecraft or probe potential (Φ) relative to the plasma potential, also known as the floating potential of each surface.

It is important to note that PSP is in a mesothermal plasma environment with plasma ion thermal velocities lower than the SW (~300km/s) and spacecraft speeds (up to 197 km/s), and plasma electron thermal velocities that remain greater than the spacecraft and solar wind velocities. A spacecraft in a mesothermal plasma forms a wake behind it [*Wang et al. '92, Ergun et al. '10, Wang et al. '18*].

Photoemission, emitted electrons that escape from a surface where an energetic photon has impacted, is material, solar flux and angle of incidence dependent [*Feuerbacher et al. '72, Garrett '81, Whipple '81, Hastings et al. '96*]. As will be shown below, because of the increase of photon flux to the surface at all wavelengths due to $1/R^2$ increase from aphelion to perihelion, and the expected densities and temperatures of the ambient plasma, the photocurrent is the highest current that illuminates surfaces of PSP experience.

The dependence of photocurrent on floating potential depends on the relative dimensions of the emitting surface (SC or antenna) and the Debye lengths of the surrounding plasma. In what follows, we assume that the Debye lengths are large compared to the relevant dimensions of the SC and the antennas, and we'll show that that's the case for the PSP electron environments. If the Debye lengths are smaller than the dimensions of the SC and antennas, as we will show for the photoelectrons and SE, the currents and floating potentials can be approximated by assuming the shape to be a flat surface. The following equation is used to find the photocurrent if the Debye length is greater than the spacecraft dimensions (thick sheath approximations) [*Grard '73*]:

$$I_{ph} = A_s J_{ph0} G_{ph}\left(a, r, \eta_{ph}\right) \text{ for } \Phi > 0 \quad (2)$$

and

$$I_{ph} = A_s J_{ph0} \text{ for } \Phi \leq 0 \quad (3)$$

where J_{ph0} is the saturated photoelectron current density, A_s is the effective illuminated area and the factor G_{ph} is dependent on the shape of the probe [*Mott-Smith et al. '26*], as seen in Figure 2, and is defined for general species j as:

$$G_j(\eta_j) = \begin{Bmatrix} 1 + \eta_j & Sphere \\ \frac{2}{\sqrt{\pi}}\sqrt{\eta_j} + e^{\eta_j}\,\mathrm{erf}\left(\sqrt{\eta_j}\right) & Cylinder \\ 1 & Flat\ Surface \end{Bmatrix} \quad (4)$$

The scaled η_j shown in the following equation:

$$\eta_j = \frac{q_j \Phi}{k_b T_j} \quad (5)$$

where, q_j is the species charge, k_b is the Boltzmann constant and T_j is the species temperature. The cylindrical equation is used for actual flight antenna model verification. The cylinder in SPIS is considered as a thin wire, where the length L (~2m) is much greater than the radius R (1.6 mm) and end effect corrections are neglected.

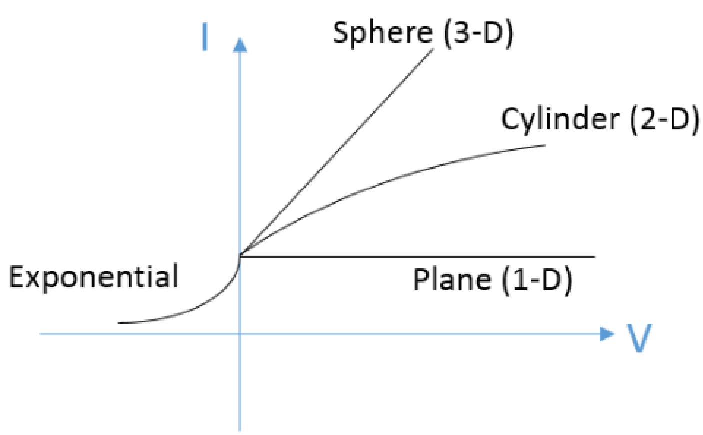

Figure 2 Thick sheath or orbit limited current voltage behavior

Past measured J_{ph0} have ranged from 20 to 60 μA/m^2 at 1 AU, which is often several times the flux observed in ground experiments [*Ergun et al. '10*]. The FIELDS antennas and shields, composed of Nb-C103, have a tested range of J_{ph0} between 139 to 49 μA/m^2 [*Diaz-Aguado et al. '19*] depending on the material state (annealed versus unannealed) and solar cycle and activity [*Sternovsky et al. '08, Diaz-Aguado et al. '19*]. Current flight estimated Nb-C103 J_{ph0} is closer to 240 μA/m^2.

As shown below, the photocurrent is the highest current on PSP, though followed by SE currents, at one order of magnitude smaller for FIELDS and two orders of magnitude smaller for the spacecraft, reducing the influence of the material properties of SE. SE are defined as emitted electrons due to kinetic impacts with primary incident electrons or ions. For the FIELDS antennas, the ambient electron temperature of the SW is increasing from a few eV to tens of eV, in the range where the SE yield becomes greater than one, causing the departing current of SE to be greater than the arriving environment electron current. Secondary electron (ion induced) yield results in similar induced currents as the ion current due to high impact efficiencies, $I_{sei} \sim I_i$ [*Ergun et al. '10*].

SE can be approximated by an isotropic Maxwellian distribution, with a characteristic energy of T_{se}~2eV [*Hachenberg et al. '59, Lai '12, Lai '13*]. Estimates of the SE yield due to electrons have been difficult to predict theoretically, but by knowing that the yield is strictly dependent on the incoming energy and angle, we can look at J_e/n_e and material dependent J_{se}/n_e (T_e) figures to predict at what ambient electron temperatures the SE currents are greater than the electron current [*Diaz-Aguado et al. '20*]. The SE current can be calculated:

$$I_{se} = I_{se0} G_{se}(a, r, \eta_{se}) \text{ for } \Phi > 0 \tag{6}$$

where G_{se} is the shape factor and I_{se0} is the saturated SE current, defined as:

$$I_{se0} = A \frac{J_{se}}{n_e}(T_e) n_e \tag{7}$$

The scaled potential difference for SE is similar to the photoemission, as both T_{se} and T_{ph} have similar characteristic energies.

Note that past studies of the SE yield of conductive materials at temperatures greater than 600K, have shown a decrease in yield on the order of 0.05%/K [*Warnecke '36, Sternglass '54, Michizono et al. '04*]. For the first perihelia the predicted antenna surface temperatures are ~885 K, and the yield reduced by 44% relative to results at 270-300 K; for the closest perihelia, the expected decrease in SE yield is even greater, on the order of 79 % [*Diaz-Aguado et al. '20*].

These temperature-dependent effects were not modeled in this analysis as photocurrent dominated the current balance by an order of magnitude.

Ambient electron currents are in the same order of magnitude as SE. Assuming the region of plasma has zero potential, and if the potential of the probe is negative relative to the nearby plasma, then the Maxwellian thermal electron current is given by:

$$I_e = I_e^0 \, e^{\eta_e} \quad \text{for } \Phi \leq 0 \tag{8}$$

where I_e^0 is defined as

$$I_e^0 = Aen_e\sqrt{\frac{k_b T_e}{2\pi m_e}} \tag{9}$$

n_e is the ambient electron density, m_e is the electron mass. If the surface potential is positive, then the electron current is calculated with the following equation:

$$I_e = I_e^0 G_e(a, r, \eta_e) \text{ for } \Phi > 0 \tag{10}$$

Where the factor G_e is dependent on the shape, see eq. 6 and η_e shown in eq. 7.

In contrast with the Maxwellian electron population in the SW, the ions can be considered as a cold, nearly monoenergetic beam. The velocity of the SW varies depending on the distance from the Sun and solar activity, but it is in the range of 300km/s, corresponding to a proton kinetic energy of 1-2keV in the spacecraft frame. This means that the SW can penetrate barriers as high as 1-2kV [*Ergun et al. '10*], and as shown by other modelling studies, narrow negative potential wake forms behind a cylindrical body. [*Engwall et al. '06*, *Guillemant '14*]. In this study, these are found to be three orders of magnitude smaller than the photoemission current, and calculated simply:

$$I_i = Aen_i u_0 \tag{11}$$

where A is the surface impinged by the beam, n_i is the ion number density, u_0 is the combined ram and ambient medium velocity

The BSE current is in the same order of magnitude as the ion current. BSE occur when electrons impact and enter the surface, but through collisions they eventually reverse direction to leave the material. The currents can be similarly calculated as the SE currents but using J_{bse}/n_e (T_e) figures. In this study, the BSE are defined as those SE backscattered with energies above 50eV[*Katz et al. '77*]. This definition is the most commonly used in the spacecraft charging community, and necessary to define material properties for NASCAP and SPIS.

As PSP approaches the Sun with each orbit with a smaller perihelion, the TPS and instruments could experience sufficiently hot temperatures to undergo thermionic emission during the closest perihelion passes. The FIELDS instrument thermal predictions have temperatures reaching 1600K, and thermionic emission becomes a primary current with similar orders of magnitude to photoemission. This thermionic current can be calculated using the Richardson-Dushman Law [*Richardson '13*, *Modinos '82*], and assuming similar orbit limited behavior:

$$I_{therm} = A_{TS}\, J^0_{therm} G_{therm}\left(a, r, \eta_j\right) \text{ for } \Phi > 0 \tag{12}$$

and

$$I_{therm} = A_{TS} J^0_{therm} \text{ for } \Phi \leq 0 \tag{13}$$

where A_{TS} is the total surface area, G_{therm} is a shape factor and J^0_{therm} is defined as:

$$J^0_{therm} = A\, T^2 e^{-\frac{\phi}{k_b T}} \tag{14}$$

where A is the material specific Richardson constant, k is the Boltzmann constant, T is the surface temperature (in eV), ϕ is the work function of the metal, and G_{therm} is the fraction of the thermionic electrons that escape as a function of surface potential, surface radius and sheath radius. The temperature of the thermionic electron leaving the surface is assumed to be 2eV, similar to SE and photocurrent electron emission temperatures.

For FIELDS, we only have the workfunction of Nb C103 [*Diaz-Aguado et al. '19, Diaz-Aguado et al. '20*] and not the Richardson Constant, A. The analysis presented uses the value of A for pure Nb to obtain the thermionic current of the antenna.

The Richardson Constant A varies significantly between materials and within the same material depending on measurement method. For example, for pure Nb, two different research measurements gave values of A between 32.7 and 57 ($A/cm^2/K^2$) [*Fomenko '56*].

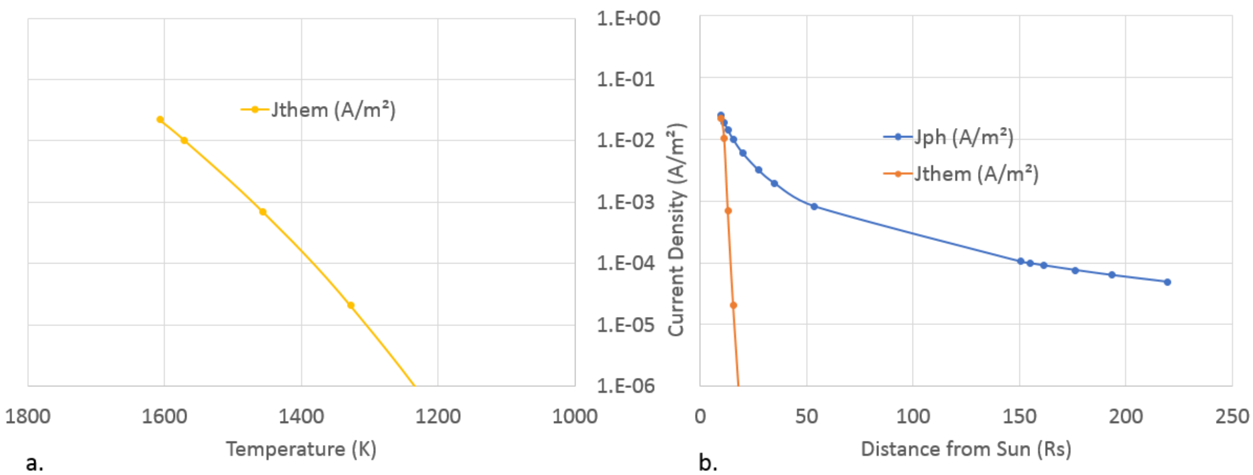

Figure 3 Thermionic emission current density of Nb-C103 – a. versus temperature of antenna, b., versus distance from the Sun comparing it with the photoemission current density.

Figure 3, a., shows the predicted thermionic electron current emitted by the antenna during the mission as the spacecraft perihelion decreases in altitude. Figure 5, b. shows the thermionic and photoemission current density of the antenna versus the distance to the Sun. While the thermionic current from the antenna was not included in this study because of issues with the current SPIS version (6.0.0), one can see that at heliocentric distances of 30-40Rs, the thermionic current is at least 4 orders of magnitude less than the photoelectron current, and so has not significant effect on the model results shown below.

3 SPIS Software and Numerical Simulations

The PSP charging models shown below were implemented using the SPIS package [*Thiebault '13*]. New materials and material properties were added to the SPIS database.

SPIS is an electrostatic unstructured 3D mesh, particle in cell (PIC), plasma modeling software, that uses JAVA, making it highly modular. SPIS provides a modeling framework to build up the antenna and spacecraft geometry and materials, the plasma environment and the interaction between them. It then uses the Vlasov-Poisson equations to self-consistently solve for the potential distribution, Φ, including the potentials on the FIELDS antenna, FIELDS shield and spacecraft surfaces. For example, the time independent Vlasov equation is shown in the following equation:

$$\boldsymbol{v} \cdot \nabla f + \frac{q}{m}(\boldsymbol{E} + \boldsymbol{v} \times \boldsymbol{B}) \cdot \frac{df}{dv} = 0 \qquad (20)$$

Where v is the velocity of the particle, f is the distribution function, E is the electric field, B is the magnetic field, q is the particle charge, m is the particle mass. To obtain the potential of the spacecraft or probe, we use Poisson's equation:

$$\nabla^2 \Phi = -\frac{\rho}{\varepsilon_0} = -\frac{\sum_i \; q n_i}{\varepsilon_0} \quad (21)$$

where ε_0 is the permittivity and the current is the summation of different particle densities, where n is the number density given by the following distribution function equation:

$$n(x,t) = \int f(\boldsymbol{x}, \boldsymbol{v}, t) d^3 v \quad (22)$$

where x is the position of the particle, v its velocity, t is the time elapsed.

The software uses a particle-in-cell, or PIC approach, in which it is important to specify a sufficiently small simulation time step Δt. This Δt should be selected to ensure that the fastest particles in the simulation move less than one simulation cell in a single time step. It should also be smaller than the plasma characteristic timescale, or the plasma period $T_p=1/\omega_{pe}$, where ω_{pe} is the plasma frequency, and can be calculated using the following equation:

$$\omega_{pe} = 8.93x10^3 \; n_e^{1/2} \quad (23)$$

For PIC simulations, the plasma Δt should be less than $0.2T_p$ to ensure proper modeling of the electric fields and avoid modeling erroneous electron oscillations.

SPIS offers the use of various velocity distribution functions, *f*, for the particles. For ambient electron an isotropic, non-drifting Maxwellian distribution function was used:

$$f(v) = \frac{n}{\left(\sqrt{2\pi} v_{th}\right)^3} exp(-v^2/2v_{th}^2) \quad (24)$$

where v_{th} is the average thermal velocity.

While past observational results have found that the ambient electron distributions are better described by heavy-tailed Kappa distributions rather than a Maxwellian [*Maksimovic et al. '05, Gloeckler et al. '06, Halekas et al. '08, Leitner et al. '09, Pierrard et al. '10, Guillemant '14*], prior modeling efforts have utilized Maxwellian electrons, and so our study will also in order to better facilitate comparison with those prior modeling results.

From this modeling framework and results, various case studies in different operational regimes are used to provide a full set of predictions for antenna, spacecraft, and antenna-spacecraft plasma interactions on PSP FIELDS.

As shown in Figures 5 and 6, the PSP spacecraft and FIELDS antennas have unique shapes, driven by the requirement to protect the thermally sensitive portions of the instruments and spacecraft from the radiant heat of the Sun. PSP's sun facing side consists of a thermal protection system (TPS, or sun and heat shield) that protects the rest of the spacecraft. The TPS is attached to a Ti frame that holds the spacecraft radiators and four of the FIELDS antennas. As shown in Figure 5, the FIELDS antennas and shields were first stowed along the spacecraft body in order to fit them within the launch fairing and secure them against launch loads and vibration. They were later deployed and are exposed to the solar flux and SW.

The FIELDS antennas had their own small Sun shields near the spacecraft to be able to reduce the heat flux going from the antennas to the instrument electronics. We modeled and analyzed the deployed state of the antennas as follows.

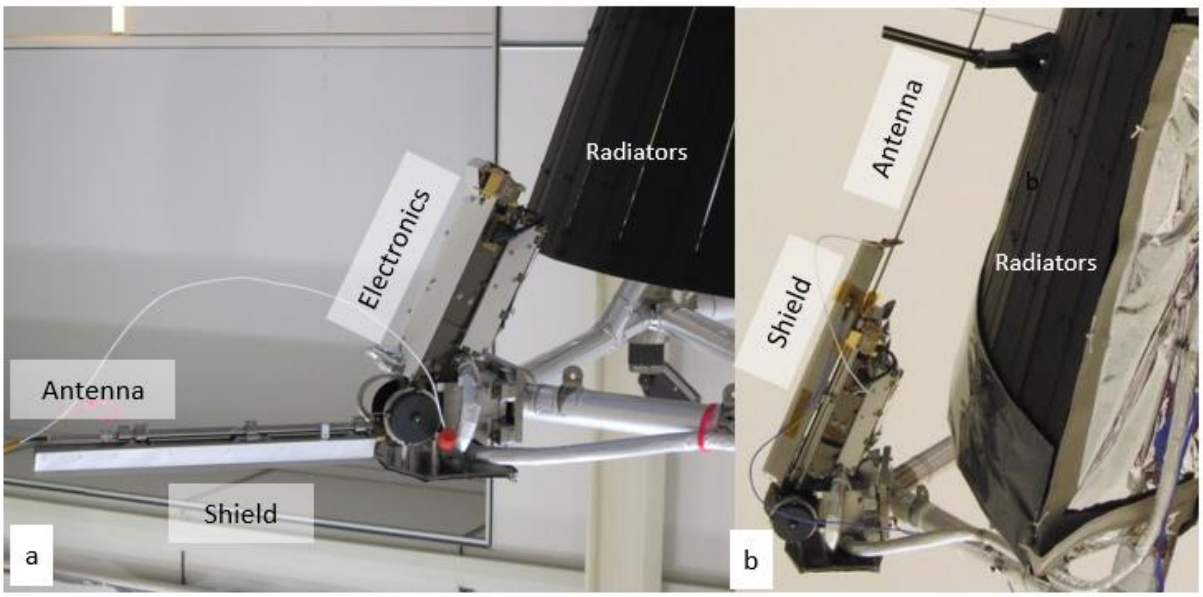

Figure 5 FIELDS instruments on the spacecraft during integration and testing a. Deployed state b. Stowed state

As shown in Fig. 6, a simplified geometry was used in SPIS for the spacecraft body, TPS, FIELDS shield and antenna. A 1 m diameter and 1 meter long, cylinder with similar outside surfaces was used for the spacecraft (in actuality it is hexagon prism). The solar panels were not modeled, as this paper was mostly concerned about the FIELDS antennas. The solar arrays were not modeled, as the arrays were mostly in the shade at 35Rs, and the dominating current of the spacecraft was the photoelectron emission of the TPS.

The radiators were modeled as a cone, with the top diameter of 1 m, bottom diameter of 2m, and 1 m tall. The TPS was also modeled as a flattened cone, with a thickness of 0.12m, 2.48 m bottom diameter, 2.44 top diameter. The Alumina face shield on the TPS was modeled as a thin layer covering the entire Sun facing side of the TPS. A FIELDS antenna was modeled as 1-D wire, as the diameters are much smaller than the length, 0.0032m diameter versus 2m length. The FIELDS Sun shield was modeled as a trigonal trapezohedron (0.32m long, 0.02m wide), with surface exposures similar to the two thin welded elements of the actual Sun shields.

Because of meshing convergence difficulties due to geometries of the model, only one shield and one antenna were modeled, and several cases run with different orientations of the ram velocity, 90° and 180°, at the first perihelion (35Rs), to reveal any differences in charging.

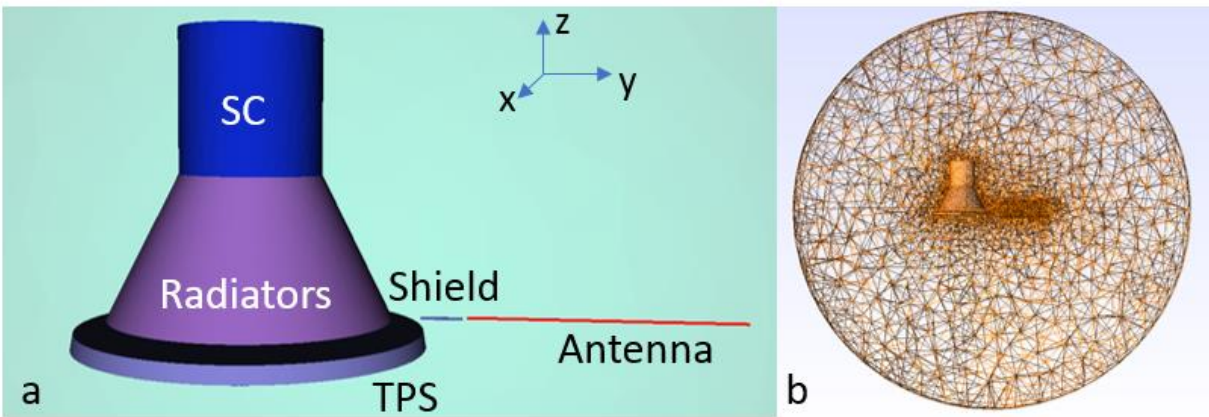

Figure 6 spacecraft model in SPIS a. Groups (except the side TPS facing the Sun) b. Mesh

Figure 6b shows the simulation unstructured mesh, with a size of 1m at the sphere, 10cm at the spacecraft, 8cm at the TPS, 1cm at the shield and 3cm at the antenna. The spacecraft model is centered within a 16-m radius simulation volume, at least twice the Debye length of the plasma environment, and tens of times the effective Debye lengths of the photoelectron and SE populations. Figure 6 also shows the x,y,z axis, with the z axis aligned with the spacecraft away from the Sun, y axis aligned with the antenna, and x forming a right-handed triad with y and z. A finer mesh, as seen in Table 5, was used for 9.5Rs to ensure that the Debye length was greater than the mesh cell near the spacecraft, ensuring that the grid was less than half the Debye length in the sheath.

Table 1 shows the modeled properties of the antenna and spacecraft materials, including photocurrent, SE yield properties, backscattered electron properties, and conductivity (bulk and surface). The antenna and antenna shield both consist of Nb C103, the TPS shield consists of Al_2O_3 (alumina), the TPS of Carbon-Carbon foam, the radiators were coated with black conductive paint (BWCondPaint), and the spacecraft was mostly covered in conductive black Kapton Multi Layered Insulation (MLI) blanket and few white conductive radiators.

The ion SE yield properties of Nb-C103 were not known at the time of publishing, instead the properties of Aluminum were used. Given that the ion current is small, this assumption has no significant effect on the modeling results. The average photoelectron yield values between solar maximum and solar minimum were used for both the Nb-C103 annealed and unannealed. The photocurrents are predicted to vary by up to +/-17% for the unannealed Nb-C103 and +/-15% for the annealed Nb-C103, depending on solar activity [*Diaz-Aguado et al. '19*]. Table 2 shows the variable conductivity of Al_2O_3 due to temperature. As the spacecraft nears the Sun, the temperature of the Alumina increases, and its conductivity increases, improving the electrical connection between the illuminated and shadowed portions of the TPS and spacecraft.

Table 1– Material Properties used in Surface Charging Calculations [*Thiebault '13, Donegan et al. '14, Diaz-Aguado et al. '20*]

	Spacecraft	*Radiators*	*TPS Foam*	*TPS-Shield*	*FIELDS shield and antenna*	
Node #	0	0	0	1	Antenna 2/ Shield 3	
Material	BlackKapton	BWCondPaint	Carbon Foam	Al_2O_3	NbC103 Unannealed	NbC103 Annealed
Diaelectric Constant				9.6		
Thickness(m)				1e-4		
Bulk Conductivity (Omega $^{-1}$ m $^{-1}$)	Cond	Cond	Cond	***	Cond	Cond
Effective Atomic Number	5	6.1	4.5	10.2	44.1	44.1
Delta-Max	2.1	1.42	0.93	6.4	1.81	1.97
E-Max (keV)	0.15	0.26	0.28	0.45	0.269	0.252
Range 1 (Angstrom)	71.48	1	180	5	0.733	0.867
Exponent 1	0.6	1.7	0.45	0.1	0.584	0.46
Range 2 (Angstrom)	312.1	1.3	312	1	1.0	1.0
Exponent 2	1.77	0.7	1.95	2.5	1.78	1.71
Proton Yield	0.455	0.287	0.455	0.68	0.244**	0.244**
Proton Max (KeV)	140	1000	80	60	230**	230**
Photoemision (A/m2)	5.00E-06	N/A	N/A	7.80E-05	1.18e-4* +/-0.204e-4	5.75e-5* +/-0.09e-4
Surface Resistivity (omega/square)	Cond	Cond	Cond	***	Cond	Cond
Richardson Dushman	N/A	N/A	N/A	N/A	37.2	37.2

Constant						
Work function	N/A	N/A	N/A	N/A	4.48	4.35

*Average solar min/max photocurrent
**Properties not available at the time of publication, used Aluminum instead
***Used Table 2 for Al_2O_3 conductive properties as they are thermally dependent, and therefore dependent on distance to the Sun.

As shown in Fig. 7, the charging model consists of 4 different groups of surfaces, or nodes: spacecraft, Radiators and TPS- foam were node 0, TPS-Sun is node 1, FIELDS Shield is node 2, FIELDS antenna is node 3. As shown in Table 1, the spacecraft, Radiators and TPS foam are considered all to be Node 0. Node 1 is the TPS shield and is connected to Node 0 through a variable resistor, which is dependent on the electrical properties of alumina, as shown in Table 2. Node 2 is the antenna and Node 3 is the antenna shield.

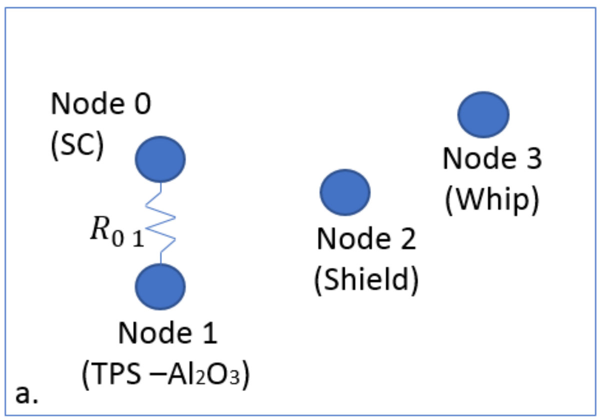

Figure 7 Model circuit design: Circuit with floating shield and whip

The models were run in two configurations: First, Node 2 and Node 3 were free floating for all environmental cases; second, Node 0 and Node 3 and Node 0 and Node 2 were connected with a variable differential voltage for the first perihelion pass environments only to model the conditions during the inflight I-V bias current sweeps, shown in Part II. The authors would like to note that the current future closest approach will be at 9.8Rs, compared to the modeling results shown at 9.5Rs. The modeling results have a 6% higher radiant flux and photoelectrons flux, which increases the number of electrons leaving compared to current estimated closest approach, influencing the photocurrents but with a small impact on the potential trends.

Table 2 – Conductivity and Resistivity Properties of Al_2O_3 [*Donegan et al. '14*]

Alumina Electrical Properties	*Bulk Conductivity ($Ohm^{-1}\ m^{-1}$)*	*Surface Resistivity (Ohm/square)*

0.045AU (Previous Final Perihelion), 9.5Rs	Cond.	Cond.
0.1AU (Science Ops.), 20Rs	Cond.	Cond.
0.16AU (First Perihelion), 35Rs	1E-06	Cond.
0.25AU, 54Rs	6.00E-09	6.00E+11
0.73AU (Venus) 155Rs	1.00E-15	1.00E+19
1AU, 215Rs	1.00E-15	1.00E+19

PSP is exposed to the SW plasma environment near the Sun's equatorial plane. Table 3 summarizes the predicted parameters of that plasma environment during various phases of the PSP mission. The response of the ambient electrons, PE, and SE to the potential structures around the spacecraft and antennas was modeled using PIC. The SW ions were also modeled using PIC.

To account for the great changes in PSP orbital velocity from aphelion to perihelion, the SW ion velocity in the spacecraft frame was modeled differently depending on the distance from the Sun. As the spacecraft nears perihelion, the velocity increases, as shown in Table 3. Near the Earth and Venus, the velocity vector of the SW had a 45 deg angle in the z-y plane. At science operations (0.25AU and closer) the SW was more radial, in the z direction, and the velocity of the spacecraft was perpendicular to it in the y or ram direction.

Table 3 – Expected Plasma Parameters of PSP FIELDS Space Environment [*Bale et al. '16*]

		1 AU	*0.72 AU (Venus)*	*0.25AU*	*1st Perihelion*	*Science Ops*	*Final Per.*
Plasma Parameter	Units	215 Rs	155 Rs	54 Rs	35 Rs	20 Rs	9.5 Rs
Electron Num. Density	cm^{-3}	6.93	13.5	116	281	881	4022
Proton Temperature	eV	8	11.2	30.7	39.9	55.8	87.1
Electron Temperature	eV	8.14	10.4	23	31.8	48.3	84.3
Magnetic Field Intensity	nT	5.8	9.72	67	157	476	2102
SW Speed	km/s	363	349	308	292	273	250
Spacecraft Velocity	km/s	15.8	30.6	74.4	96.8	134	197
Debye Length	m	8	6.5	3.3	2.5	1.7	1.1
Electron Gyroradius	m	1660	1119	241	121	49	14
Ion Acoustic Velocity	km/s	39.5	44.7	66	78	96.2	127

It is worthy to note that the ambient electron Debye length decreases as the distance from the Sun decreases and is within the same dimensions of the spacecraft and FIELDS antennas during perihelion passes. The photoelectron and SE Debye lengths also decrease as the distance from the Sun decreases but are smaller than the dimensions of the spacecraft. These Debye's lengths are shown in the results.

SPIS uses super-particles injected in each cell to represent dynamics of individual groups of particles. The smaller number of super-particles are easier to track and make the PIC processing less intensive. Each of them represents a group of physical particles ruled by physics. For this analysis, super-particle numbers per cell ranged between 10 and 15 for electrons and ions, 5 for photoelectrons, 3-2 for SE, 1-2 for BSE and ion induced SE, totaling 9.3 million super-particles for 35Rs, and 16.4 million super-particles for 9.5Rs. Figure 8 shows the number of super particles run in the model for a typical 35Rs run. Steady state was reached around 1e-4 sec. The usual computational run-time was 8 hours for 35Rs with 24 threads, 2.9GHz, 32GB memory computer. At 1AU the computational time was at least 4 days due to the low conductivity between the TPS shield and the spacecraft.

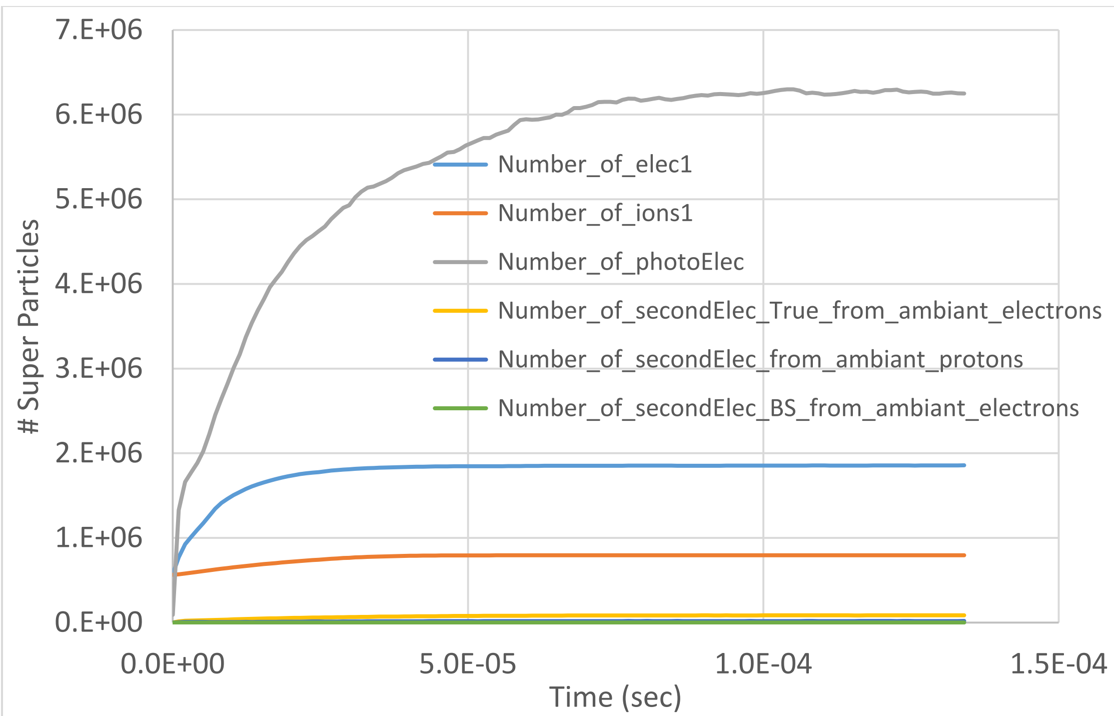

Figure 7 Super Particle # versus Simulation Time for 35Rs

As shown in Table 4, different ram directions (0°, 90° and 180°) in the x-y plane were studied at 35Rs, in order to discern any aspect-dependent charging effects on the antennas or spacecraft. For reference, the Sun is at -z direction.

Table 4 – Graphical representation of different Ram direction cases

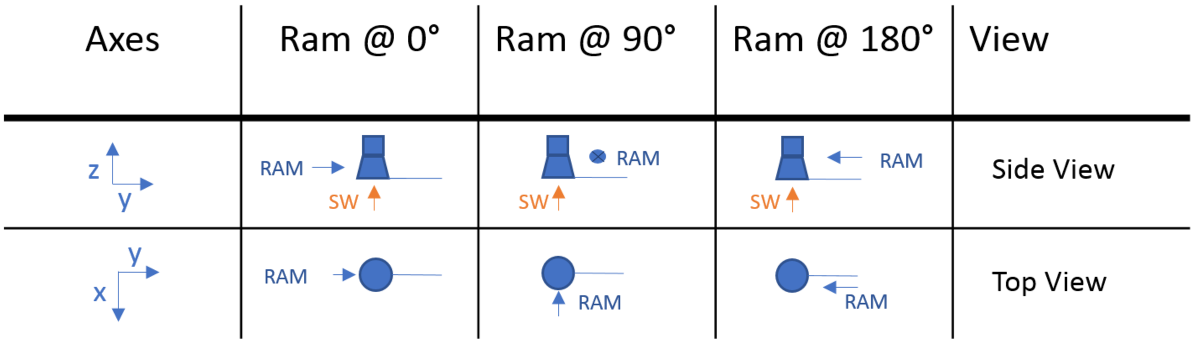

Table 5 shows the major numerical inputs from the SPIS runs and typical mesh size. The timestep (Dt) was held smaller than usual because the mesh had tetrahedron angles smaller than 60deg. The capacitance of the spacecraft was held at 2x10^{-10} F, but was varied to slow/speed up modeling results. Table 3 also shows the electron plasma frequency, Debye lengths and electron gyrofrequencies.

Table 5 - Typical Numerical Settings for SPIS

	1AU - 35Rs	*9.5Rs*
Electron Dt and Duration	5e-8 s	1e-8 s
Ion Dt and Duration	5e-7 s	1e-7 s
SE and Photoem. Dt and Duration	5e-8 s	1e-8 s
Plasma Dt and Duration	5e-7 s	1e-7 s
Ion/Electron Super Particle/cell	10-15	10-15
Photoemission Super particle/cell	5	5
SE Super particle/cell	4	4
SE Ion Super particle/cell	3	3
Sphere Mesh Size	1 m	1 m
Spacecraft Mesh Size	0.1 m	0.03 m
TPS Mesh Size	0.09 m	0.04 m
Shield Mesh Size	0.01 m	0.01 m
Antenna Mesh Size	0.03 m	0.03 m

4 Results

4.1 Numerical Results Unbiased FIELDS Antenna and Shield

Tables 6 and 7 show the floating potentials (i.e. potential of surface relative to the potential of the outer simulation boundary fixed at 0V) of the SC, Radiators, TPS, FIELDS antenna and FIELDS shield, for heliocentric distances and predicted plasma conditions from

1AU to 0.0495AU (9.5Rs), and for both unannealed and annealed photoelectron and SE yields. All models included a magnetic field, but it had little effect on the spacecraft and FIELDS instrument potentials from models run with no magnetic field. Studies by [*Guillemant et al. '17*] showed how ~30 times the magnetic field expected for Solar Orbiter (0.25AU) changed the potential of the Radio and Plasma Wave (RPW) antennas by only a few volts, and so the relative insensitivity of the model to B-field effects is consistent with past results.

In these runs, one can see that the floating potential of the spacecraft and TPS were highly dependent on the conductance of the Alumina. At closer distances to the Sun, the TPS and spacecraft floated to similar potentials as shown in Table 6 and 7. At Earth and Venus where the Alumina temperature is predicted to be markedly lower and significantly more resistive, this significant isolation resistance allows the shadowed spacecraft to charge negative as the current from the ambient electrons and SE is higher than the ambient ions, while the illuminated TPS charges positive due to high photoelectron currents. Table 6 also shows the effect of changes in the ram direction of the SW as described in Table 4, , and of reductions of SE yield due to temperature increases of the surface.

Table 6 – Surface Potentials (V) for PSP FIELDS Space Environment (unannealed Nb C103)

	219 Rs (Earth)	*155 Rs (Venus)*	*54 Rs*	*35 Rs RAM 0°/90°/180°*	*35* Rs *(SEY Red.)*	*20* Rs	*9.5* Rs	*9.5* Rs *(SEY Red.)*
SC	-12.4	-14.5	0.90	6.63/6.63/6.05	6.05	0.65	-13.0	-12.8
Radiator	-12.4	-14.5	0.90	6.63/6.63/6.05	6.05	0.65	-13.0	-12.8
TPS Foam	-12.4	-14.5	0.90	6.63/6.63/6.05	6.05	0.65	-13.0	-12.8
TPS Shield	14.8	6.75	4.85	6.35/6.40/6.25	6.25	0.65	-13.0	-12.8
FIELDS Shield	23.0	21.8	9.60	11.8/12.2/12.5	12.5	8.75	0.92	1.4
FIELDS Antenna	29.3	27.5	13.8	17.5/17.9/17.5	17.5	16.3	14.9	14.8

Table 7 – Surface Potentials (V) for PSP FIELDS Space Environment (annealed Nb C103)

	1 AU	*0.72 AU (Venus)*	*0.25AU*	*35Rs*	*20Rs**	*9.5Rs*
Spacecraft	N/A	-14.5	0.75	6.25	0.60	-13.1
Radiator	N/A	-14.5	0.75	6.25	0.60	-13.1
TPS Foam	N/A	-14.5	0.75	6.25	0.60	-13.1
TPS Shield	N/A	6.43	4.70	6.35	0.60	-13.1
FIELDS Shield	N/A	15.6	6.45	9.1	5.75	-4.79
FIELDS Antenna	N/A	20.5	7.15	13.5	13.0	7.8

The proximity of the ion wake negative potential to the antenna at Ram 0° had minor effects on the antenna, a few tenths of a volt of change. The direction of the ion flow had very little influence on the floating potentials of any of the surfaces. This isn't surprising given the 3 orders of magnitude difference between the dominant photoelectron, SE, and ambient electron currents and the ion currents.

Spacecraft floating potential does not depend significantly upon the FIELDS antenna and shield characteristics and their floating potentials as can be seen by comparing Table 5 with Table 6. Spacecraft floating potentials were similar to predictions, except for 9.5Rs which was more negative. [*Donegan et al. '14*] modeled the slow and fast SW at different heliocentric distances, predicting spacecraft floating potentials at 0.25AU between -0.2V and 9.2V, at 35Rs between 1.0V and 8.0V, and at 9.5Rs between -3.3V and -8.8V. For the 35Rs, the spacecraft potential predictions are within past models, but for the 9.5Rs case, the potential of the spacecraft is more negative. [*Donegan et al. '14*] also modeled an extreme, post shock-case, with a spacecraft floating potential prediction of -31V.

The annealing effects in Table 6 show the floating potential of the shield and antenna lower than the unannealed cases as expected given the reduced PE yield of the annealed materials. The spacecraft material properties and dimensions stayed constant, while the PE yield of the antenna and shield materials were reduced by annealing, decreasing their floating potentials and that of the spacecraft as well; as fewer electrons leave the shield and antenna surfaces, the potential becomes less positive to maintain current balance.

Table 8 shows the current source comparison between 1AU (215Rs) and 0.16AU (35Rs) for unannealed Nb-C103. At 219Rs the total currents are two order of magnitude smaller than at 35Rs. The photocurrent is dominating in both cases, by two orders of magnitude at 219Rs and by one order of magnitude at 35Rs. The SE current is two orders of magnitude smaller at 219Rs compared to 35Rs, which is only one order of magnitude smaller for the entire spacecraft, including the antennas. The ion current is two orders of magnitude smaller than the photocurrent at 1AU, while it is up to three orders of magnitude smaller at 0.16AU. The SE due to ions are in the same order of magnitude as the ion current. The BSE currents are also small, several orders of magnitude smaller than the photoemission and not an important factor in the current balance in both environments.

As explained in the materials section, the high temperature on the antennas could have effects on their potentials by reducing the SE current. The potential differences are shown in Table 5-6, while the currents are shown in Table 5-8. The SE currents are reduced on the FIELDS antenna by 44% at 35Rs because of the SE yield reduction due to temperature, but with similar potential results. The spacecraft potential is negative at 219Rs as it is isolated from the TPS shield, compared to the positive charging of the TPS and FIELDS instrument. At 35Rs, the TPS shield becomes more conductive, making the spacecraft dependent on the photocurrent of the TPS and charge positive.

Table 8 - Current Source Comparison for PSP between 1AU and 0.16AU.

	PSP		*FIELDS Antenna Only*		
*Current Units in **Amps***	1AU 219Rs	0.16 AU 35Rs	1AU 219Rs	0.16AU 35Rs	0.16AU (Reduced SEY)
Total Collected	-3.8E-04	-1.6E-02	-7.6E-07	-3.0E-05	-3.0E-05
Total Emitted	-3.8E-04	-1.6E-02	-7.6E-07	-3.0E-05	-3.0E-05
Collected Electron	-7.4E-06	-7.9E-04	-3.7E-08	-1.2E-06	-1.0E-06
Collected Ion	1.9E-06	6.5E-05	1.5E-09	7.0E-08	1.1E-07
Collected Photoelectron	-3.6E-04	-1.4E-02	-7.0E-07	-2.8E-05	-2.8E-05
Collected SE	-4.9E-06	-1.0E-03	-2.5E-08	-1.6E-06	-1.3E-06
Collected BSE	-1.5E-07	-6.5E-06	1.0E-10	-3.5E-08	-1.3E-08
Collected SE Ion	-1.2E-06	-3.8E-05	-4.5E-10	-2.0E-08	-2.0E-08
Emitted Photoelectron	-3.7E-04	-1.5E-02	-7.4E-07	-2.9E-05	-2.9E-05
Emitted SE	-6.3E-06	-1.2E-03	-2.6E-08	-1.4E-06	-9.0E-07
Emitted SE Ion	-1.6E-06	-3.9E-05	-5.9E-10	-1.5E-08	-1.7E-08

Figure 8 shows the potential in volts on two slices through the simulation domain at steady state, allowing the reader to see both the surface potentials on the spacecraft, TPS, antenna, and shield, along with the potential distribution in the plasma surrounding those surfaces during the first perihelion. The spacecraft charges positively at about 6.2 V, while the antenna and shield float even more positive (+17.5 V and +11.8 V relative to outer simulation boundary, respectively). Negative potential wells with a depth of -3.25 V form in front of the TPS and in the ion wake of the spacecraft, not as deep as those previously found at 9.5Rs by [*Ergun et al. '10, Guillemant et al. '12, Donegan et al. '14*]. These wells do differ in depth and dimension from those observed in previous studies because previous studies focused on 9.5Rs, while this research focused on 35Rs. At 35Rs, the photoemission fluxes are lower as the solar flux is lower, the electron and ion number density and temperature, are lower, which translate also to lower SE fluxes. That said, [*Ergun et al. '10, Guillemant et al. '12, Donegan et al. '14*] found the negative potential well in front of the TPS was less deep than the wake potential well.

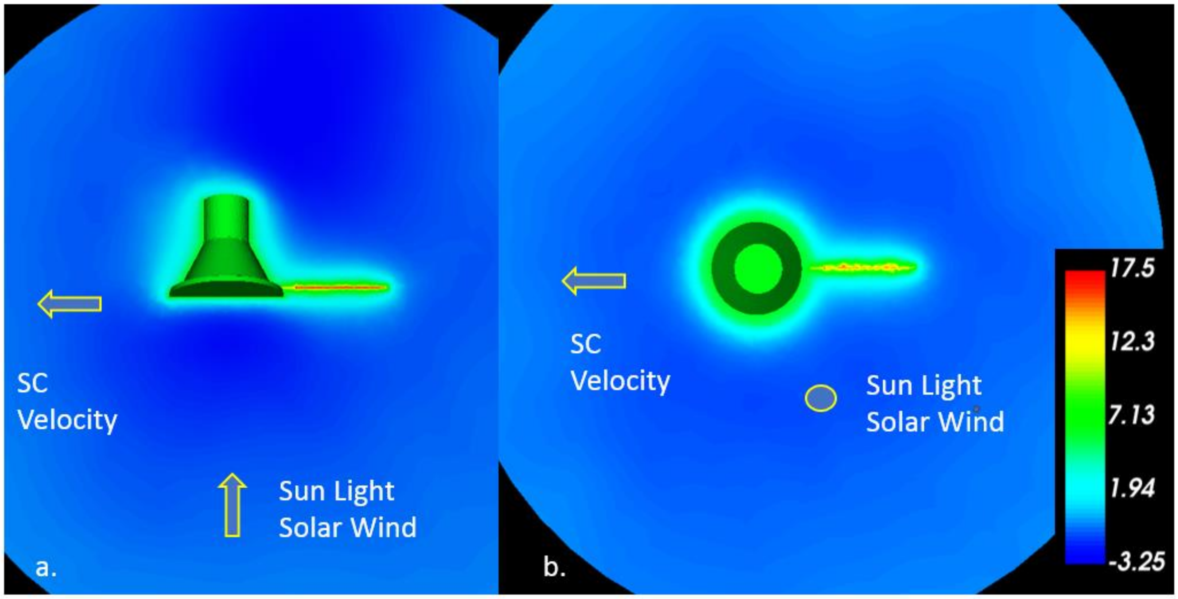

Figure 8– Slice of the Steady State Plasma Potential (Volts) and Spacecraft and FIELDS Potential (Volts) at 35Rs (First Perihelion) a. y-z plane, b. x-y plane

Figure 9 shows these differences in a comparison between our runs at 35Rs and 9.5Rs. Note that the color scales for the potential are different between the two cases in order to show the extent and depth of the potential wells. In these cases, [*Donegan et al. '14*] predicted negative wake potential wells charging from -20V to -36V, compared to -23.9V in Figure 5-6, but their plasma parameters varied from the ones in this study with their densities ranging from 1.2×10^3 cm^{-3} to 4.1×10^4 cm^{-3}, electron temperatures ranging from 48.6eV and 59.7eV, and ion temperatures ranging from 40.5eV to 223.1eV.

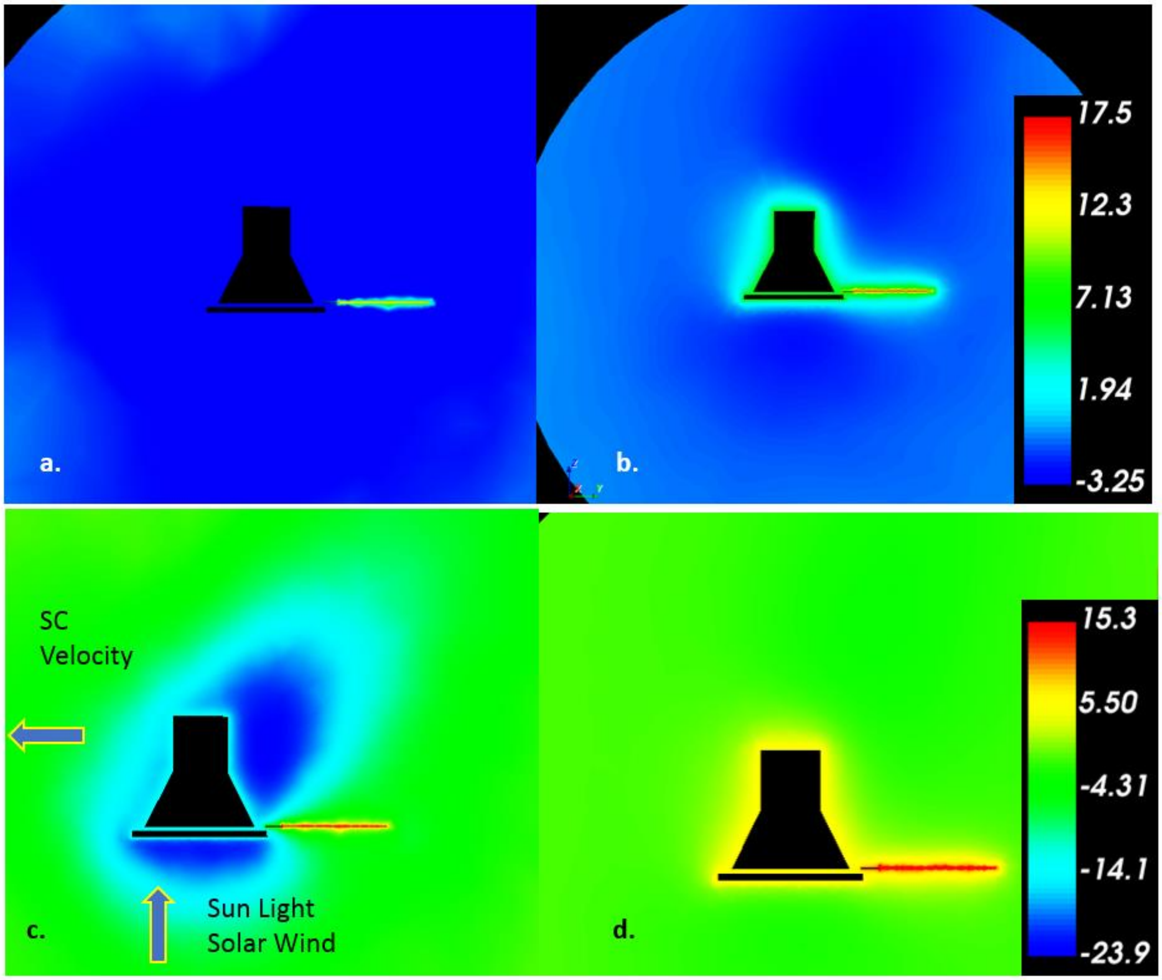

Figure 9 Plasma Potential (Volts) of PSP a. and c. 9.5Rs, b. and d. 35Rs, a. and b. at 35Rs potential scales and c. and d. at 9.5Rs potential scales

The plasma potential around the shield (a.) and the antenna (b.) are shown in Figure 5-9, for the antenna at 90° RAM. The antenna and shield wakes at 0° RAM case join the wake of the spacecraft and therefore are not discernable and more negative.   Similarly to the TPS in Figure 5-5, a negative potential well forms in front of the shield and the antenna. Note that the well in front of the antenna is not as negative as the shield and TPS. The wake from the significant proton flow (solar wind plus PSP orbital velocity) can also be seen. Note that the well in front of the antenna is not as negative as the shield and TPS.

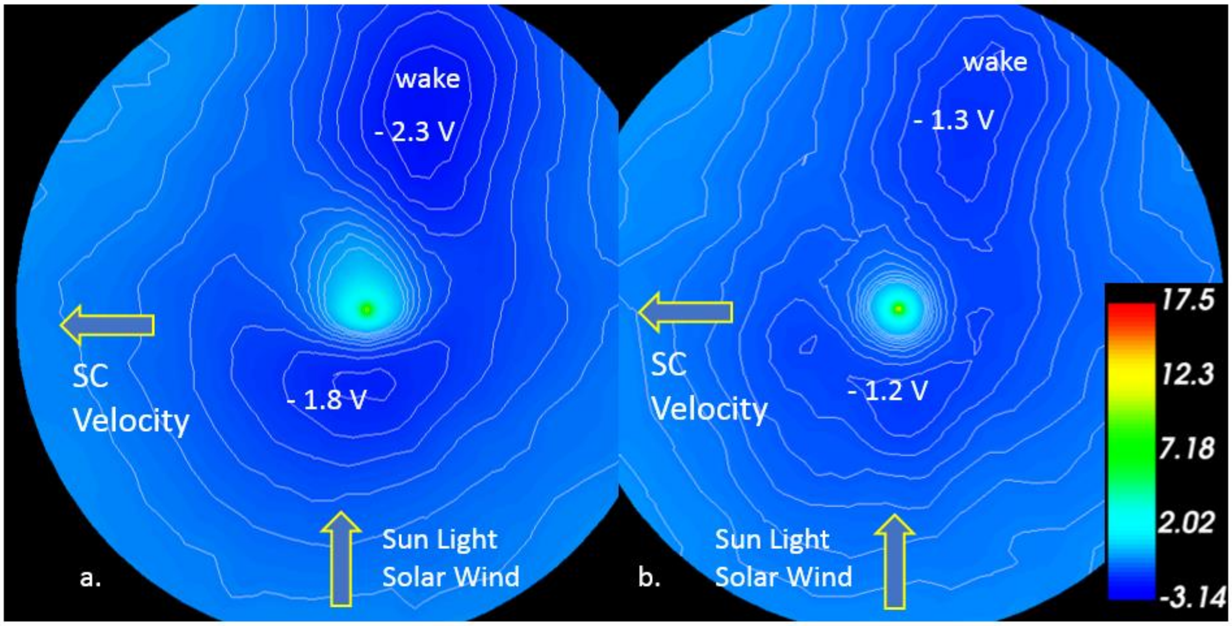

Figure 10 Plasma Potential (Volts) of the cross-sections of the a. shield and b. antenna – at 90° ram, diameter of the spherical boundary is 16m

Figure 11 to 17 show the plasma characteristics and the near spacecraft plasma environment of a cross-section of the PSP and the antenna at 1AU (219Rs), on the left, and at 0.16AU(35Rs) on the right. Figure 11 shows the plasma potential of PSP and the antenna in Volts. The negative potential well in front of the TPS and antennas are not seen at 1AU compared to 0.16AU. The wake potentials are also different due to a different angle of attack of the ions, and lower density of the ions at 1AU. The TPS shield and the spacecraft are isolated from each other at 1AU and charging at different potentials. At 35Rs the TPS shield and spacecraft charge to similar potentials. The FIELDS antennas decrease their potential. All potentials are shown in Table 6.

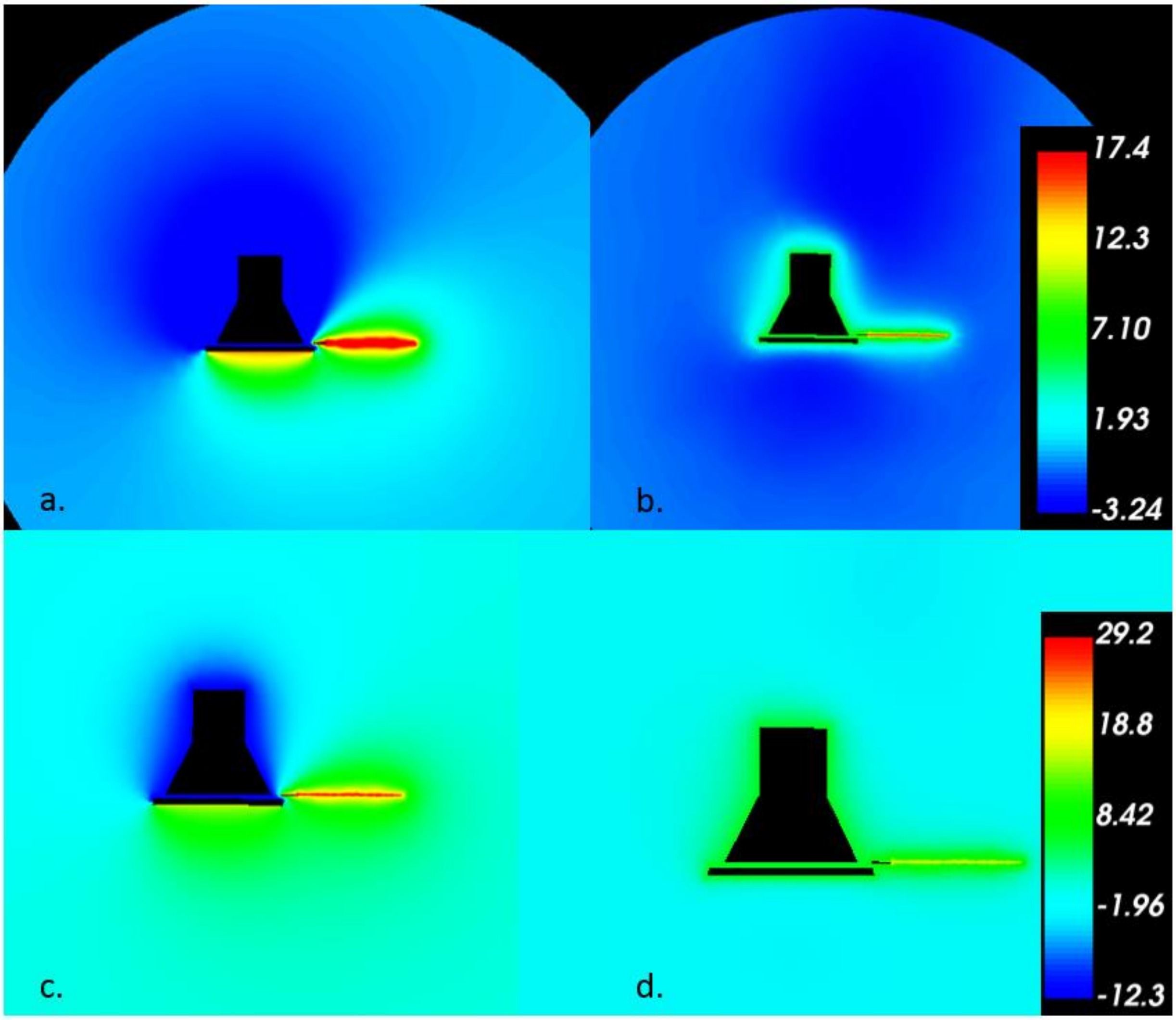

Figure 11 Plasma Potential (Volts) of PSP a. and c. 219Rs (1AU), b. and d. 35Rs (0.16AU), a. and b. at 35Rs potential scales and c. and d. at 1AU potential scales

Figure 12 shows the Log electron plasma charge density. The electron density increases as the spacecraft approaches the Sun. The electron number density figure at 1AU (left) is smoother due to a larger scale, compared to the 35Rs figure (right) which has a much smaller scale. Figure 13 shows the ion number density. The wake is seen in both 1AU and 0.16AU, but as the velocity of the spacecraft increases, the wake has a larger ram component. The ion number density is shown with a linear scale to better capture the wake structure. A low-density ion region forms opposite the impinging ions from the ram and solar wind. Higher electron mobility leads to negative space charge filling the wake, which forms a negative potential area, as seen in previous simulations [*Ergun et al. '10, Guillemant et al. '12*]. The negative potential well in front of the TPS supported by PE and SE populations, as well as the one in the wake supported by ambient, PE, and SE electrons, repel ambient electrons, leading to reduced ambient electron densities in those locations, as seen in Figure 12 b.

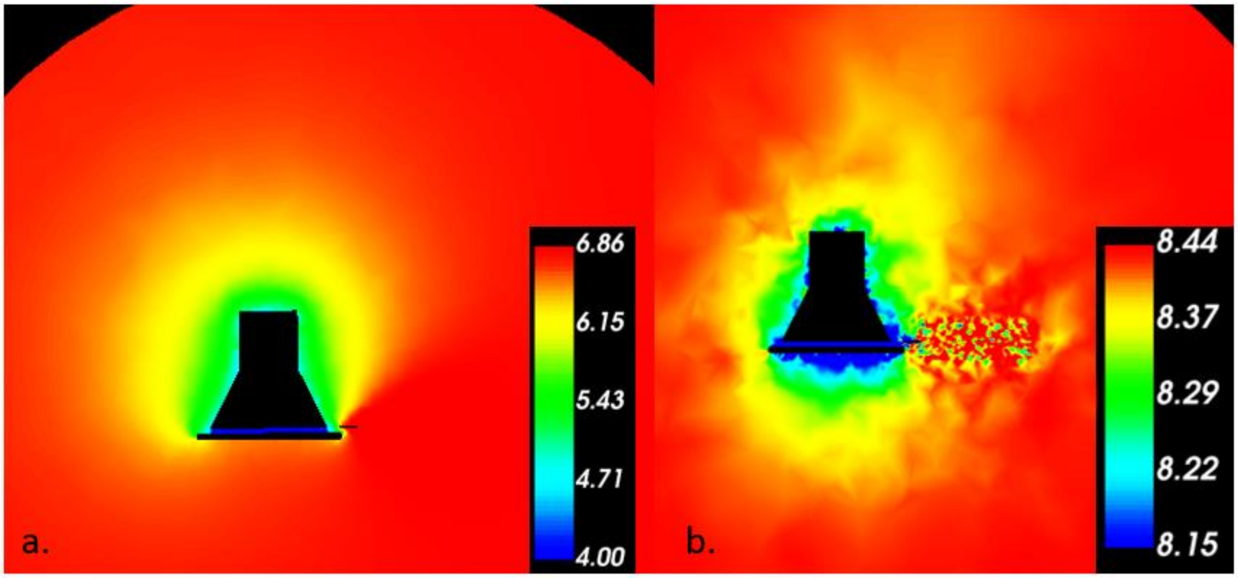

Figure 12 PSP and FIELDS Log Electron Number Density (log (#/m^3)), a. 1AU and b. 0.16AU

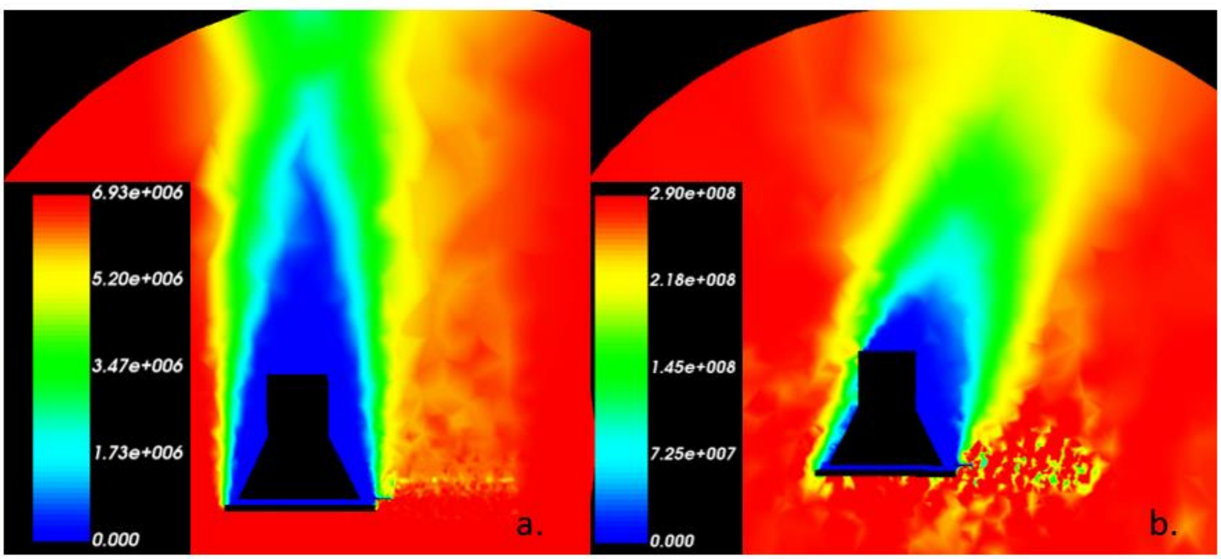

Figure 13 PSP and FIELDS Ion Number Density (#/m^3), a. 1AU and b. 0.16AU

Figure 14 shows the photoelectron number density. The photoelectron density is much higher for 0.16AU as expected, as it is closer to the Sun. The photoelectrons produced fill the wells in front of the TPS and to a lesser degree, the antenna well. Figure 5-14 shows the SE charge density. The SE number density is one order of magnitude smaller than photoelectron number density at 0.16AU.

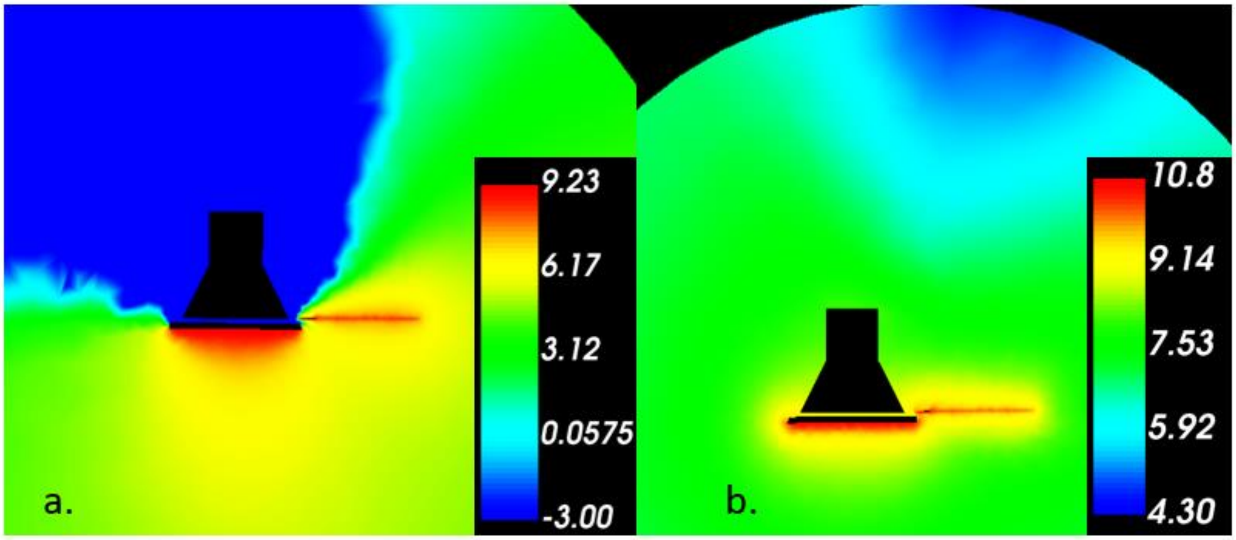

Figure 14 PSP and FIELDS Log Photoemission Number Density log (#/m^3), a. 1AU and b. 0.16AU

It is important to note that near the antenna and TPS, the photoelectron number density is one order of magnitude greater than the SE number density, and two orders of magnitude greater than the ambient electrons and ions. Compared to the spacecraft, the antenna and its shield are exposed to the Sun and are photoelectron current dominated. The photoemission electron number density (~1e10 1/m^3) is the highest of all particle densities by at least an order of magnitude within a region several meters away from the spacecraft and antennas. Figure 14 shows how the photoelectrons at 35Rs occupy the environment near the spacecraft, compared to that at 1AU, where it concentrates mainly on the TPS and the antenna. Similarly, Figure 15 shows the electrons occupying the near spacecraft environment at 35Rs, in contrast to 1AU, where a singular structure forms around it. The SE concentrate in front of the TPS shield, near the antenna, close to the side of the spacecraft and in the wake. It is significant to note that the Debye lengths are shorter at 35Rs than at 1AU.

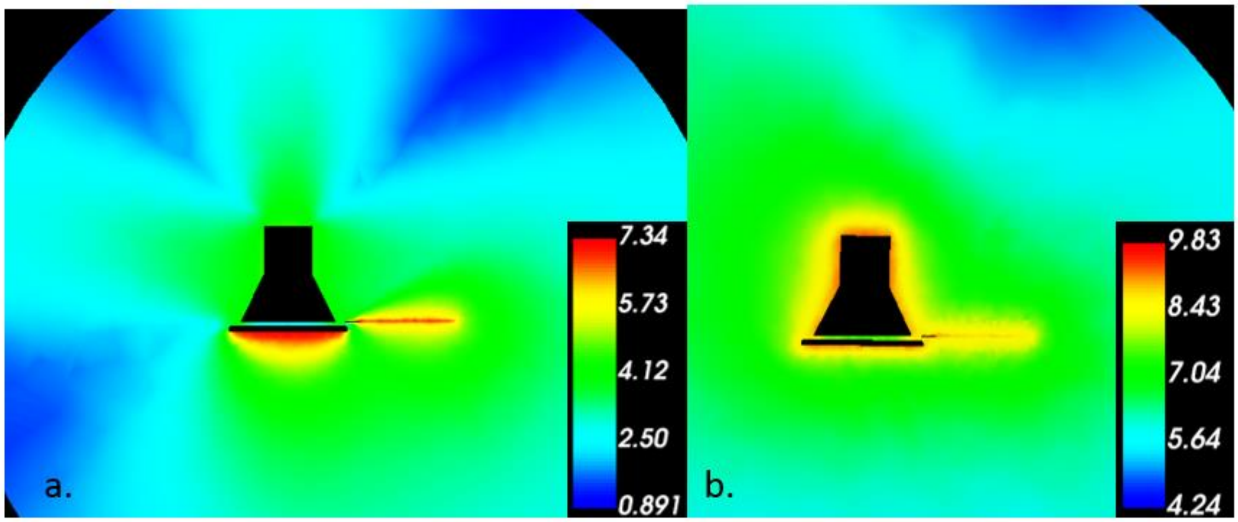

Figure 15 PSP and FIELDS Log SE Number Density log (#/m^3), a. 1AU and b. 0.16AU

Figure 16 shows the BSE charge density, at two orders of magnitude smaller than photoelectron density. The BSE are attracted to the TPS shield and antennas which are charging positive at both 1AU and 0.16AU. Figure 5-16 shows the ion SE charge density, also at two orders of magnitude smaller than the photoelectron charge density. At 1AU the ions hit the left corner of the spacecraft, causing a small ion SE source. At 35Rs, the ions impact a larger surface, showing a larger ion SE source on the spacecraft. This difference is due to the greater ram velocity at 35Rs.

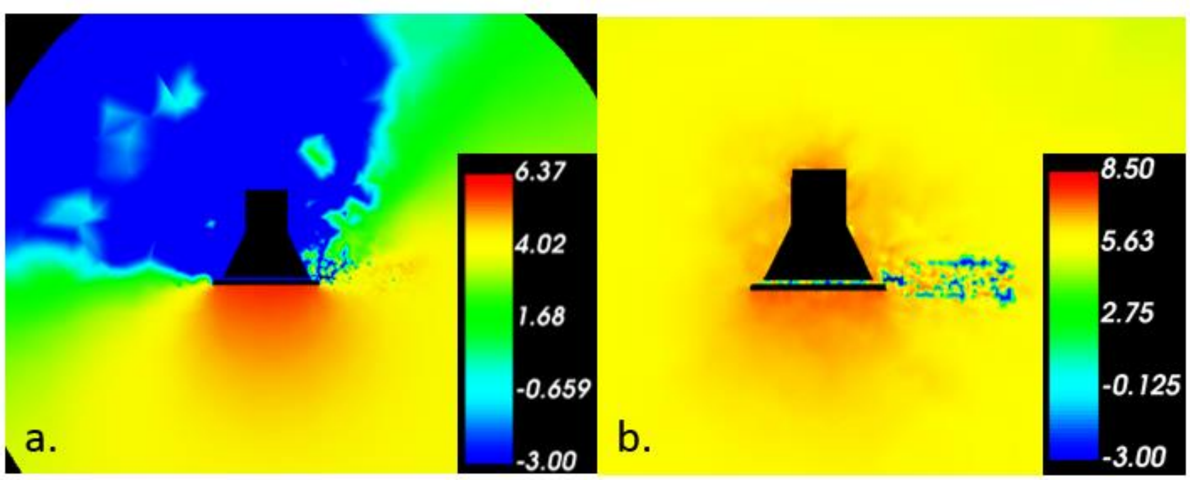

Figure 16 PSP and FIELDS Log BSE Number Density log (#/m^3), a. 1AU and b. 0.16AU

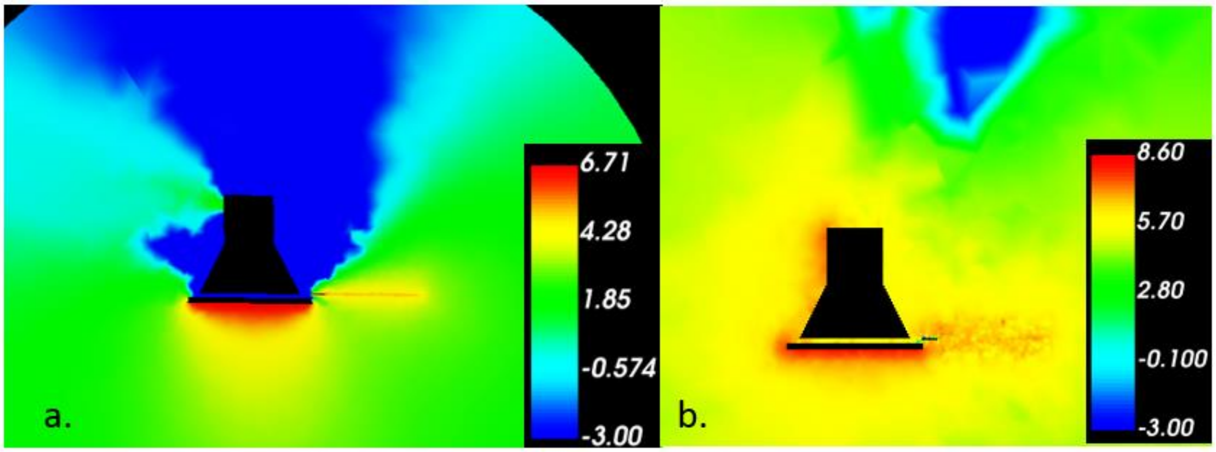

Figure 17 PSP and FIELDS Log SE Number Density due to Ions log (#/m^3), a. 1AU and b. 0.16AU

Figure 18 shows the particle densities in front of the TPS as a function of distance for 1AU, 0.16AU and 0.045AU. The TPS shield is located at -0.2m. It also includes the potential as a function of distance. For 0.16AU and 0.045 AU the potential in front of the spacecraft has virtual cathodes (negative potential wells as shown in Figures 5-8, 5-9 and 5-10). Space-charge-limited currents which cause this virtual cathode are determined by the PSP spacecraft sheath. They have been studied extensively by many authors, including Langmuir [*Langmuir '29*]. Bohm [*Guthrie '49*], Crawford and Cannara [*Crawford et al. '65*], Prewett and Allen [*Prewett et al. '76*], Marese et al. [*Ketsdever et al. '00*], Wang and Lai [*Wang et al. '97*]. Figure 18 show that the minimum of these wells occurs when the number density of the photoelectrons (plus other negative charge densities) become larger than the ion charge density, creating an inflection of the potential in the Poisson's equation, as shown in eq. 21. This inflection does not occur at 1AU. Please note that at 9.5Rs the densities have some small oscillations on the densities near the shield which could be caused by too large of a timestep.

Figure 19 shows the position of the negative well in front of the TPS, and the Debye lengths of the plasma thermal electrons, the photoelectrons and SE near the TPS versus the distance of the spacecraft with respect to the Sun. The location of the negative well gets closer to the TPS as the spacecraft nears the Sun. This occurs at a rate not dependent on the ambient thermal electron Debye lengths. It is closer to the SE and photoemission SE current reduction rates as the spacecraft approaches the Sun.

Furthermore, the SPIS results show the collected current from photoelectrons, as they return to a positive potential antenna. On an isolated free-floating antenna (i.e. without shield or spacecraft nearby), both ends would have similar values. However, photoelectrons from the shield are attracted to the antenna, making the collected current density of the antenna near the shield larger. In other words, this photoelectron current to the antenna from the shield changes the current balance and final free-floating potential of the antenna.

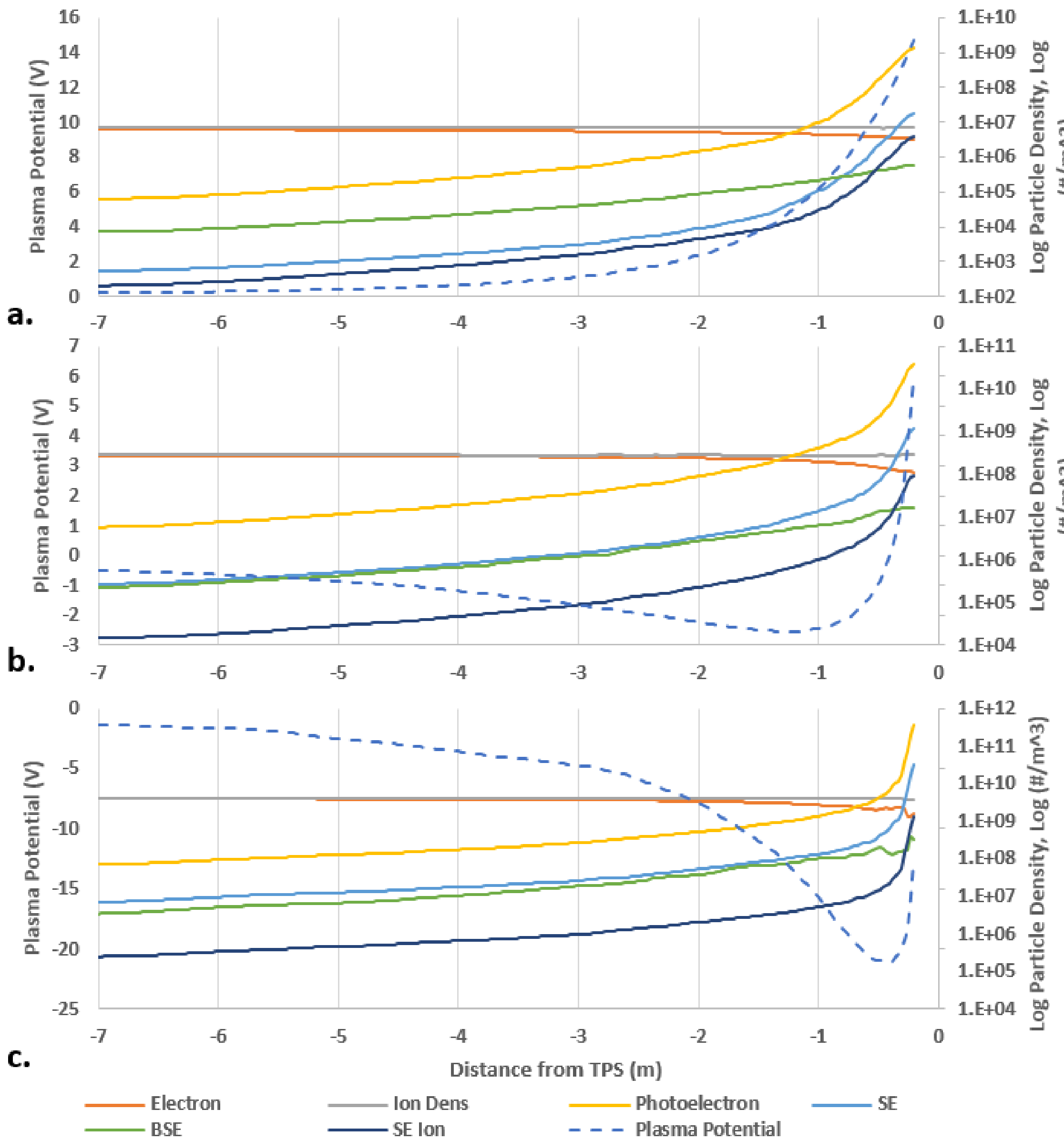

Figure 18 PSP TPS Shield Potential and Plasma Densities as a Function of Distance at a. 1AU (219Rs), b. 0.16AU (35Rs) and c. 0.045AU (9.5Rs)

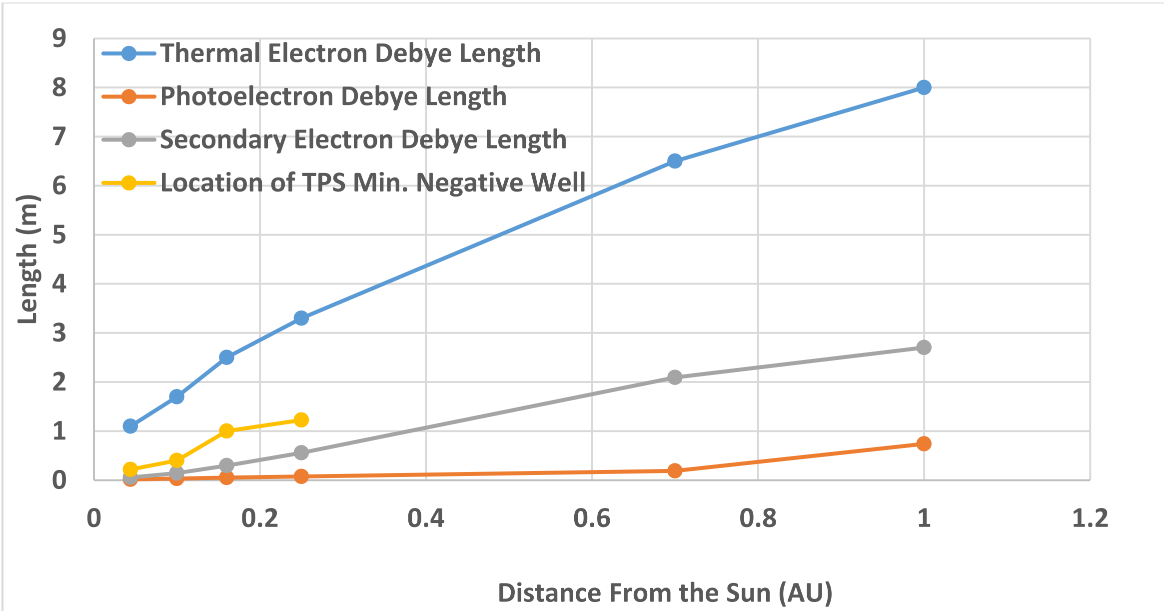

Figure 19 TPS Negative Well Position, including the Thermal Electron, Photoemission, SE Debye Lengths versus the Distance from the Sun

In addition, the modeling results show the net current density of the antenna, where the tip has positive current density while the area near the shield has negative current density. This negative density is mostly due to photoelectrons and SE both attracted from the shield. To reduce the influence of this current from the shield on the antenna's floating potential, a voltage bias is imposed between the shield and antenna, with the results shown in Part II of this paper.

4.2 Sensitivity Analysis

Various sensitivity analysis were conducted on the PSP FIELDS model to find both the main current source contributor and verify the model. A variation on electron and ion density, ion velocity, photocurrent and magnetic field were introduced in the modeling parameters at both 1AU and 35Rs. The previous section showed the differences in currents between the photoelectron yield of the FIELDS Nb-C103 annealed versus unannealed. The potentials clearly showed a dependence on the photocurrent yield, but there was also a change in the SE yield due to annealing, even though this change was less prominent. Multiple runs were performed at 1AU and 0.16 AU (35Rs) with a variation of environmental inputs.

The models were run with a variation of the distance from the Sun to vary photon flux, and hence photoemission, while keeping the electron and ion densities and velocities the same. The 1AU model (nonconductive TPS) was run at 0.7AU, double the photon flux, and hence the

Sun exposed surface photoemission, and at 1.4AU, half the photon flux. At 0.7AU the photoemission current and hence the total currents doubled. The TPS shield and FIELDS antenna and shield remained positive and attracted the electrons. Their potential though decreased by a few volts (~3 to 5V). The spacecraft potential remained equal as the electron and ion environment were not changed and the TPS and the spacecraft were isolated from each other. At 1.4AU, there was half the photon flux than at 1AU. Photocurrent also halves, decreasing the number of electrons emitted which reduces the potential of the surface. The photoelectron density decreases with respect to other electrons at 1AU. Photon flux variation was also run at 35Rs with different results, simulating the photon flux at 53Rs and 27Rs while maintaining plasma densities constant. At 35Rs, the potential of the surfaces was greater than at 53Rs and continued to increase at 27Rs. The photoelectrons increased, which increased the potential.

The model was run with no SE yield to confirm that the SE current was not a predominant influence on the potential during close encounters. At 35Rs it was found that the SE yield did not influence the potential charging greatly (minus a few millivolts on the antenna and minus one volt on the spacecraft). Like the antenna, the shield and the spacecraft were charging positive, and the emitted electrons were attracted by the positive potential surfaces. At 1AU, the SE had a greater influence on the surface potentials, but just by a few volts (~2V). If the SE yield is removed, the spacecraft potential decreases by a few volts (~3V), the TPS shield decreases by half a volt and the antenna reduces its potential by five volts.

The models were also run with a variation of electron and ion density while keeping the photoemission constant. At 1AU, the model was run with higher ambient plasma density (by one order of magnitude). The higher density of the plasma causes the potential of the antenna, the TPS shield and the spacecraft to decrease, showing a dependency on the ambient thermal electron density. The model was also run with a smaller order of magnitude of ambient plasma density. In comparison with the higher density, the potential increased by tens of volts for the spacecraft, TPS shield, and antenna. At 35 Rs (0.16AU) similar electron and ion density variation was performed. When the electron and ion densities were doubled, the potentials decreased by few volts on the spacecraft, TPS and the antenna. The model was then run with the density halved. The potentials of the spacecraft and the antennas increased by a few volts. At 35Rs the TPS shield is conductive, making the TPS shield and spacecraft float at the same potential.

The magnetic field was also modified from expected values to see no changes at either 1AU, 35Rs nor 9.5Rs. The gyroradius of the electrons remains much larger than the spacecraft and FIELDS antenna dimensions. Changes in the magnetic field do not affect PSP and FIELDS charging.

Finally, the model was run at 35Rs with the finer mesh of 9.5Rs in order to do a comparison run. The currents and potentials were compared. The model found that for the spacecraft the difference in the total collected and total emitted current to be 0%, while for the FIELDS antenna the total collected current and emitted current difference was 0.3%. The maximum error on the spacecraft was of 3% for the collected SE, while for the FIELDS antenna it was 31% of the collected SE ion. This contrast was probably due to the reduction of the super particles which was done in order to be able to run the models in a shorter period of time. These errors had little effect on the total current and final potential of the antenna during the I-V curve models, and with the lower number of super-particles the models ran faster with the author's limited computing resources. The plots shown in the previous section were created using runs with a larger number of super particles to decrease the maximum current errors down to 7%. The average potential errors were low, with an overall average of 2.9%, and a maximum error of 8.9% on the spacecraft.

This sensitivity study of varying the photoemission yield, SE yield, electron and ion densities reinforced the importance of knowing the material properties of the PSP and FIELDS shield and antenna. Material properties of the TPS shield at high temperatures and photoemission and SE yields must be known to predict the plasma environment near the spacecraft and instrument.

5 Conclusions

The theoretical spacecraft charging overview was shown, introducing the use of thermionic emission as a primary current. The PSP spacecraft and FIELDS antennas were modeled using SPIS software to predict their potential and current interactions with the environment. Results predict the FIELDS antennas charging positive for all cases. The plasma potentials show the ion wake and negative potentials in front of the TPS, as previously predicted. The plasma potential also shows the ion wake and negative wells in front the FIELDS shields and antennas. The antenna had a shallower negative potential well surrounding the cylinder, but similar negative potential well due to ion wake. It is important to note, the spacecraft potential predictions were within past estimates, except at 9.5Rs, which was closer to an extreme SW event. Finally, a sensitivity analysis was performed which reinforced the importance of knowing the material properties of the FIELDS antenna and the rest of the spacecraft to predict the potential charging of the antenna.

Acknowledgments, Samples, and Data

Millan D.A. would like to thank David Glaser, Chris Scholtz, Marc Pulupa at Space Sciences Laboratory. He would also like to thank Julien Forest, Benjamin Ruard, Arnaud Trouche, and Jean-Charles Mateo Velez for their SPIS modeling feedback. This work was partially supported by the NASA PSP FIELDS contract NNN06AA01C. Flight and environmental data used in this paper are publicly available at http://fields.ssl.berkeley.edu/data. Model data are available at Zenodo, TBD link.

References

1 Andersson, L., et al. (2015). "The Langmuir Probe and Waves (LPW) Instrument for MAVEN." Space Science Reviews **195**(1): 173-198.
2 Bale, S. D., et al. (2016). "The FIELDS Instrument Suite for Solar Probe Plus." Space Science Reviews **204**(1-4): 49.
3 Bonnell, J. W., et al. (2008). "The Electric Field Instrument (EFI) for THEMIS." Space Science Reviews **141**(1): 303-341.
4 Crawford, F. W., et al. (1965). "Structure of the Double Sheath in a Hot-Cathode Plasma." Journal of Applied Physics **36**(10): 3135-3141.
5 Diaz-Aguado, M., et al. (2019). "Experimental Investigation of Total Photoemission Yield from New Satellite Surface Materials." AIAA Journal of Spacecraft and Rockets **56**(1): 248-258.
6 Diaz-Aguado, M. F., et al. (2020). "Experimental Investigation of the Secondary and Backscatter Electron Emission from New Spacecraft Surface Materials." AIAA Journal of Spacecraft and Rockets **TBD**(TBD).
7 Donegan, M. M., et al. (2014). Surface Charging Predictions for Solar Probe Plus. Spacecraft Charging Technology Conference. Pasadena. **134**.
8 Donegan, M. M., et al. (2010). "Spacecraft Coating-Induced Charging: Materials and Modeling Study of Environmental Extremes." Journal of Spacecraft and Rockets **47**(1): 134-146.
9 Engwall, E., et al. (2006). "Wake formation behind positively charged spacecraft in flowing tenuous plasmas." Physics of Plasmas **13**(6).
10 Ergun, R. E., et al. (2010). "Spacecraft charging and ion wake formation in the near-Sun environment." Physics of Plasmas **17**(7): 072903.
11 Feuerbacher, B., et al. (1972). "Experimental Investigation of Photoemission from Satellite Surface Materials." Journal of Applied Physics **43**(4): 1563-1572.
12 Fomenko, V. S. (1956). Handbook of Thermionic Properties. New York, Plenum Press Data Division.
13 Fox, N., et al. (2016). "The Solar Probe Plus Mission: Humanity's First Visit to Our Star." Space Science Reviews **204**(1-4): 7-48.
14 Garrett, H. B. (1981). "The charging of spacecraft surfaces." Reviews of Geophysics **19**(4): 577-616.
15 Gloeckler, G., et al. (2006). "Anisotropic beams of energetic particles upstream from the termination shock of the solar wind." The Astrophysical Journal **648**(1): L63-L66.

16 Grard, R. J. L. (1973). "Properties of the satellite photoelectron sheath derived from photoemission laboratory measurements." Journal of Geophysical Research **78**(16): 2885-2906.

17 Guillemant, S. (2014). Study and simulations of spacecraft/plasma interaction phenomena and their effects on low energy plasma measurements, Université Paul Sabatier-Toulouse III.

18 Guillemant, S., et al. (2012). "Solar wind plasma interaction with solar probe plus spacecraft." Annales Geophysicae **30**(7): 1075.

19 Guillemant, S., et al. (2017). "A Study of Solar Orbiter Spacecraft-Plasma Interactions Effects on Electric Field and Particle Measurements." IEEE Transactions on Plasma Science **45**(9): 2578-2587.

20 Gurnett, D. A., et al. (2004). "The Cassini Radio and Plasma Wave Investigation." Space Science Reviews **114**(1): 395-463.

21 Gurnett, D. A., et al. (1995). "The Polar plasma wave instrument." Space Science Reviews **71**(1-4): 597-622.

22 Gustafsson, G., et al. (1997). "The Electric Field and Wave Experiment for the Cluster Mission." Space Science Reviews **79**(1): 137-156.

23 Guthrie, A. (1949). The characteristics of electrical discharges in magnetic fields. R. K. Wakerling. New York, McGraw-Hill.

24 Hachenberg, O., et al. (1959). "Secondary Electron Emission from Solids." Advances In Electronics And Electron Physics **11**: 413-499.

25 Halekas, J. S., et al. (2008). "Lunar Prospector observations of the electrostatic potential of the lunar surface and its response to incident currents." Journal of Geophysical Research: Space Physics **113**(A9).

26 Hastings, D., et al. (1996). Spacecraft-Environment Interactions. New York, Cambridge University Press.

27 Katz, I., et al. (1977). "NASCAP, a Three-Dimensional Charging Analyzer Program for Complex Spacecraft." IEEE Transactions on Nuclear Science **24**(6): 2276-2280.

28 Ketsdever, A., et al. (2000). Micropropulsion for Small Spacecraft. Reston, American Institute of Aeronautics and Astronautics.

29 Lai, S. T. (2012). Fundamental of spacecraft charging: spacecraft interactions with space plasmas. Princeton, N.J., Princeton University Press.

30 Lai, S. T. (2013). "Spacecraft charging: incoming and outgoing electrons." CERN Yellow Report **2**: 165-168.

31 Langmuir, I. (1929). "The Interaction of Electron and Positive Ion Space Charges in Cathode Sheaths." Physical Review **33**(6): 954-989.

32 Leitner, M., et al. (2009). "Introducing log-kappa distributions for solar wind analysis." Journal of Geophysical Research: Space Physics **114**(A12): n/a-n/a.

33 Maksimovic, M., et al. (2005). "Radial evolution of the electron distribution functions in the fast solar wind between 0.3 and 1.5 AU." Journal of Geophysical Research: Space Physics **110**(9): <xocs:firstpage xmlns:xocs=""/>.

34 Mandell, M. J., et al. (2005). "Modeling the charging of geosynchronous and interplanetary spacecraft using Nascap-2k." Advances in Space Research **36**(12): 2511-2515.

35 Marchand, R., et al. (2014). "Cross-comparison of spacecraft-environment interaction model predictions applied to Solar Probe Plus near perihelion." Physics of Plasmas **21**(6).

36 Michizono, S., et al. (2004). "Secondary electron emission of sapphire and anti-multipactor coatings at high temperature." Applied Surface Science **235**(1): 227-230.

37 Modinos, A. (1982). Theory of thermionic emission. Surface Science Letters, Elsevier B.V. **115:** A117-A117.

38 Mott-Smith, H. M., et al. (1926). "The theory of collectors in gaseous discharges." Physical Review **28**(4): 727-763.

39 Mullen, E. G., et al. (1986). "SCATHA survey of high-level spacecraft charging in sunlight." Journal of Geophysical Research: Space Physics **91**(A2): 1474-1490.

40 Pierrard, V., et al. (2010). "Kappa Distributions: Theory and Applications in Space Plasmas." Solar Physics **267**(1): 153-174.

41 Prewett, P. D., et al. (1976). "The Double Sheath Associated with a Hot Cathode." Proceedings of the Royal Society of London. Series A, Mathematical and Physical Sciences (1934-1990) **348**(1655): 435-446.

42 Richardson, O. W. (1913). "The Emission of Electrons from Tungsten at High Temperatures: An Experimental Proof that the Electric Current in Metals is Carried by Electrons." Science (New York, N.Y.) **38**(967): 57.

43 Roussel, J. F., et al. (2008). "SPIS Open-Source Code: Methods, Capabilities, Achievements, and Prospects." IEEE Transactions on Plasma Science **36**(5): 2360-2368.

44 Sternglass, E. J. (1954). "Backscattering of Kilovolt Electrons from Solids." Physical Review **95**(2): 345-358.

45 Sternovsky, Z., et al. (2008). "Variability of the lunar photoelectron sheath and dust mobility due to solar activity." Journal of Geophysical Research: Space Physics **113**(10).

46 Thiebault, B., Mateo Velez, J-C. Forest, J., Sarrailh, P. (2013). "SPIS 5.1 User Manual."

47 Torbert, R. B., et al. (2016). "The FIELDS Instrument Suite on MMS: Scientific Objectives, Measurements, and Data Products." Space Science Reviews **199**(1-4): 105.

48 Vaivads, A., et al. (2007). "Low-frequency electric field and density fluctuation measurements on Solar Orbiter." Advances in Space Research **39**(9): 1502-1509.

49 Wang, J., et al. (1992). "Ionospheric plasma flow over large high-voltage space platforms. II: The formation and structure of plasma wake." Physics of Fluids B: Plasma Physics **4**(6): 1615-1629.

50 Wang, J., et al. (2018). "The Breakdown of the Fluid Approximation for Electrons in a Plasma Wake." Journal of Geophysical Research: Space Physics **123**(10): 8797-8805.

51 Wang, J., et al. (1997). "Virtual Anode in Ion Beam Emissions in Space: Numerical Simulations." Journal of Spacecraft and Rockets **34**(6): 829-836.

52 Warnecke, R. (1936). "Secondary Emission of Pure Metals." Journal de Physique **6**: 269-280.

53 Whipple, E. C. (1981). "Potential of Surfaces in Space." Report on Progress of Physics **44**: 1197-1250.

54 Whipple, E. C., Jr. (1965). The equilibrium electric potential of a body in the upper atmosphere and in interplanetary space - NASA-TM-X-55368, Sponsoring Organization: NASA Goddard Space Flight Center.

55 Wygant, J. R., et al. (2013). "The Electric Field and Waves Instruments on the Radiation Belt Storm Probes Mission." Space Science Reviews **179**(1): 183-220.